IEEE Access
Multidisciplinary ⋮ Rapid Review ⋮ Open Access Journal

Received 2 January 2024, accepted 23 January 2024, date of publication 8 February 2024, date of current version 15 February 2024.

Digital Object Identifier 10.1109/ACCESS.2024.3364518

RESEARCH ARTICLE

Time-Domain Analysis of Temporally and Spatially Dispersive Metasurfaces in GSTC-FDTD Frameworks

JOÃO GUILHERME NIZER RAHMEIER, (Member, IEEE), JORDAN DUGAN, TOM J. SMY, AND SHULABH GUPTA, (Senior Member, IEEE)

Department of Electronics, Carleton University, Ottawa, ON K1S 5B6, Canada

Corresponding author: João Guilherme Nizer Rahmeier (joaonizer@cmail.carleton.ca)

ABSTRACT In this paper, we propose two different methods for time-domain finite-difference analysis of uniform temporally and spatially dispersive metasurfaces using their zero-thickness sheet representations using the Generalized Sheet Transition Conditions (GSTCs). Metasurfaces are described here using their effective surface susceptibilities which are assumed to exhibit Lorentzian temporal dispersion characteristics. For both methods, the spatial dispersion of the surface susceptibilities (i.e., their dependence on the angle of incidence) are represented using the extended GSTCs presented in Rahmeier et al. (2023), Smy et al. (2023), and Dugan et al. (2023). However, the first method takes advantage of a polynomial expansion of the angle-dependent surface susceptibilities in terms of the transverse wavevector to implement spatial derivatives of the electric and magnetic polarization as well as the average field on the surface, leading to a coupled set of field equations encompassing the entire surface. Limitations for this method are presented in terms of poor conditioning for a coupled system of equations and an inconvenient extension to the higher-order expansion of the susceptibility terms. The second method lifts these limitations by solving the spatial dispersion problem in the spatial frequency domain at every time step. Both methods are validated for custom Lorentzian models and two canonical physical cells while comparing their transmission and reflection coefficients with analytical results.

INDEX TERMS Electromagnetic metasurfaces, electromagnetic propagation, finite-difference time-domain, generalized sheet transition conditions (GSTCs), Lorentz oscillator model, spatial dispersion, spatial frequency domain, surface susceptibility tensors.

I. INTRODUCTION

More recently, metasurfaces, which are arrays of sub-wavelength arrays of resonating structures, have received a lot of attention since they are capable of presenting electromagnetic characteristics not available from simple material interfaces and surfaces [4]. Therefore enabling the design of exotic functionalities like electromagnetic cloaking and holography [5], [6], besides being used for beam shaping and improving the performance of antenna designs [7], among others. The broadband scattered field computation and analysis of resonant metasurfaces is a multi-scale problem as the resonant structures themselves are sub-wavelength, while the overall metasurface is typically orders of wavelength in size. To reduce the computational complexity of brute-force simulations of metasurfaces, a compact zero-thickness sheet model based on Generalized Sheet Transition Conditions (GSTCs) has recently become popular, where the metasurface is instead described in terms of their constitutive parameters using their homogenized effective surface susceptibilities, $\bar{\bar{\chi}}$. By sacrificing the microscopic field characteristics, the zero-thickness sheet model greatly simplifies the computation of macroscopic scattered fields.

Due to resonant characteristics of the underlying resonators forming the surface, typical metasurfaces are intrinsically temporally dispersive, i.e., $\bar{\bar{\chi}}(\omega)$. Moreover, for a

The associate editor coordinating the review of this manuscript and approving it for publication was Mehmet Alper Uslu.

general metasurface, these effective surface susceptibilities may also be spatially dispersive (or non-local), where their constitutive parameters are also functions of the angle of plane-wave incidences (related to the transverse wavevector $k_{\parallel}$), i.e. $\bar{\bar{\chi}}(\omega, k_{\parallel})$. Therefore, due to the interaction of broadband incident signals with dispersive metasurfaces, the scattered time-domain waveforms are distorted in both time and space, and these interactions are thus naturally captured using time-domain analysis, typically implemented using the Finite-Difference Time-Domain (FDTD) technique.

Finite-Difference Time-Domain (FDTD) is a widely used numerical technique for simulating electromagnetic wave propagation and interactions in various media [8]. FDTD discretizes both the spatial and temporal domains of the electromagnetic field equations into finite differences, allowing for the efficient and accurate simulation of complex wave phenomena. By discretizing space and time with the Yee cell, the FDTD method becomes a versatile tool for solving Maxwell's equations without the need for complex meshes or grid structures. Despite its advantages, the Yee cell does have limitations, particularly in dealing with structures that involve small geometric features compared to the wavelength, where the Yee cell resolution may become impractically large. Nevertheless, over the years, various extensions and adaptations of the original FDTD method, such as the introduction of higher-order Yee cells or hybrid approaches with other numerical techniques, have been developed to address these challenges and further expand the method's applicability to a wide array of electromagnetic problems [9], [10], [11].

Several works have been reported in the literature on FDTD analysis if metasurfaces, particularly using their zero-thickness sheet representation via the GSTCs. In [13], the GSTCs were introduced to the FDTD scheme via electric current densities source terms in the curl equations for non-dispersive real-valued electric susceptibilities. Other non-dispersive implementations are presented in [14], [15], and [16]. In [17], Smy and Gupta introduced an explicit time-dispersive model where the electric and magnetic surface susceptibilities were described using the Lorentz model to take into account the temporal dispersion characteristics of the metasurface unit cell. In [18], authors used a rational polynomial in the temporal frequency domain to represent temporal dispersion of the surface susceptibilities and then incorporated that representation in a piece-wise linear recursive convolution method. They evaluate the surface polarizations inside an explicit method to solve the GSTCs within a regular Yee-cell-based FDTD solver. More recently, an explicit Drude dispersive model was presented in [19] and an implicit Lorentz model in [12] that was later extended for time-modulated metasurfaces in [20]. Authors in [21] presented a vector fitting procedure to represent a multi-Lorentz susceptibility form in an explicit GSTC-FDTD solver.

However, all these recent works only modeled the temporally dispersive nature of the resonating structures composing the metasurfaces, while assuming a *local* response, point by point, along the surface, i.e. *non-spatially dispersive metasurface*. In such a description, the surface susceptibilities terms are functions of the temporal frequency but represent a delta function in terms of the spatial frequency domain and are implicitly independent of the angle of incidence of the exciting fields. These approaches may be sufficient only if the resonator unit cells of the metasurfaces are deeply sub-wavelength and can be represented by angle-independent effective surface susceptibilities.

More recently, the works presented in [1], [2], and [3] showed that the constitutive parameters of the resonating cells can also change with respect to the transverse wavevector, $k_{\parallel}$ i.e., the angle of incidence of the interacting fields at the surface, especially in cases where the periodicity of the cell is not deep sub-wavelength ($> \lambda/5$, as a current rule of thumb) and close to the diffraction limit of $\lambda/2$. Thus, the surface susceptibilities ended up being dependent on the spatial frequency, which corresponds to a general *non-local* response of the cell. As part of those works, a Boundary Element method (BEM) was developed for frequency domain analysis of uniform and non-uniform, periodic and finite, flat and curved spatially dispersive metasurfaces. However, to the best of our knowledge, no GSTC-FDTD method in the literature models spatially dispersive metasurfaces.

Therefore, in this work, we present, for the first time, a GSTC-FDTD-SD framework that can simultaneously incorporate both time- and space-dispersive (i.e., TD and SD) susceptibilities. We start describing the GSTC-FDTD-TDSD method for a uniform mono-anisotropic metasurface with electric and magnetic tangential susceptibilities under TE incidence, for simplicity and base the framework on the time-dispersive tight-asymmetric cell of [12] and the extended GSTCs of [1]. We validate the methodology by comparing the reflection and transmission phases and magnitudes with their analytical solution for a custom temporally and spatially dispersive electric and magnetic Lorentzian response. Then, we present a few limitations of this method and proceed with an improved mixed Finite-Difference Time-Domain/Spatial-Frequency-Domain (Mixed GSTC-FDTD-TDSD) method that solves the GSTC implicit problem in the spatial frequency domain at each time step. This version of the method shows improved accuracy and a more straightforward form to incorporate higher-order terms in the polynomial expansion of the Lorentz parameters with respect to the transverse wavevector. Finally, the methodology is further validated using data extracted from two practical unit cell structures: the wire dipole cell and the dielectric puck Huygens' unit cell presented in [1].

II. STANDARD 2D-FDTD METHOD

Initially, we define the system setup of a standard Yee cell 2D-FDTD region and a coordinate system. Propagation will

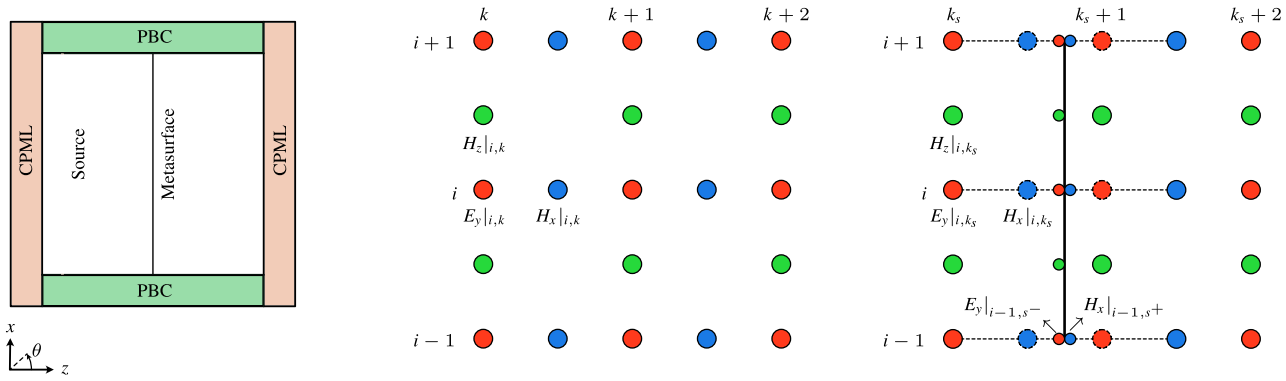

(a) Simulation Region Setup. (b) Regular Yee-cell. (c) Tight Asymmetric Cell [12].

FIGURE 1. Definition of (a) the simulation setup, (b) field nodes in the regular Yee cell, and (c) field nodes in the tight asymmetric cell from [12]. E_y components are represented by the red circles, H_x by the blue circles, and H_z by the green circles. Index i and k correspond to the x and z location of the Yee cells. The index k_s corresponds to the placement of the surface between H_x nodes at k_s and the E_y node at $k_s + 1$. Virtual nodes are created for E_y at the left of the surface (s^-) and H_x on the right of the surface (s^+).

happen in the $x-z$ plane with the angle of incidence, θ defined with respect to the z-axis. At the edges of the z-axis, we have convolutional perfectly matched layers (CPML) as absorbing boundary conditions, and at the edges of the x-axis, we have periodic boundary conditions (PBC). The overall simulation setup can be seen in Fig. 1(a).

The 2D-FDTD method is developed in Matlab using the standard FDTD equations and boundary conditions provided in [22] and [23]. For a solution in 2D with TE excitation, we are going to consider H_x, E_y, and H_z field components with no variation along the y direction, for simplicity. Hence, Maxwell's curl equations in free space with no impressed current sources are

$$\frac{\partial E_y}{\partial t} = \frac{1}{\epsilon_0}\left(\frac{\partial H_x}{\partial z} - \frac{\partial H_z}{\partial x}\right) \tag{1a}$$

$$\frac{\partial H_x}{\partial t} = \frac{1}{\mu_0}\frac{\partial E_y}{\partial z} \tag{1b}$$

$$\frac{\partial H_z}{\partial t} = -\frac{1}{\mu_0}\frac{\partial E_y}{\partial x}. \tag{1c}$$

This set of equations can be discretized using regular Yee-cells shown in Fig. 1(b) whose finite difference form using Forward Euler for time derivatives and space derivatives in E and Backward Euler for space derivatives in H, as

$$E_y|_{i,k}^{n+1} = E_y|_{i,k}^{n} + \frac{\Delta t}{\epsilon_0 \Delta z}\left(H_x|_{i,k}^{n+\frac{1}{2}} - H_x|_{i,k-1}^{n+\frac{1}{2}}\right) - \frac{\Delta t}{\epsilon_0 \Delta x}\left(H_z|_{i,k}^{n+\frac{1}{2}} - H_z|_{i-1,k}^{n+\frac{1}{2}}\right) \tag{2a}$$

$$H_x|_{i,k}^{n+\frac{1}{2}} = H_x|_{i,k}^{n-\frac{1}{2}} + \frac{\Delta t}{\mu_0 \Delta z}\left(E_y|_{i,k+1}^{n} - E_y|_{i,k}^{n}\right) \tag{2b}$$

$$H_z|_{i,k}^{n+\frac{1}{2}} = H_z|_{i,k}^{n-\frac{1}{2}} + \frac{\Delta t}{\mu_0 \Delta x}\left(E_y|_{i+1,k}^{n} - E_y|_{i,k}^{n}\right), \tag{2c}$$

where ϵ_0 is the free space permittivity, μ_0 is the free space permeability, Δt is the time step, and Δx and Δz are the space steps along the x and z directions, respectively, while the space indices i and k are used to index the respective Yee-cells while keeping the physical half space step different between E and H field. Using the leap-frog approach, the fields can be updated by first computing H values at half-time steps with past values of E and then proceeding with E field calculations at integer time steps using past values of H.

III. TIME-DOMAIN GENERALIZED SHEET TRANSITION CONDITIONS

The generalized sheet transition conditions (GSTC) rely on the zero thickness model presented by Idemen in [24]. Assuming the surface normal to be $\hat{\mathbf{n}} = \hat{\mathbf{z}}$, parallel directions $\hat{\mathbf{x}}$ and $\hat{\mathbf{y}}$ and the transverse gradient operator as $\nabla_\parallel = [\frac{\partial}{\partial x}, \frac{\partial}{\partial y}, 0]$, we can then, write the GSTC's as follows:

$$\hat{\mathbf{z}} \times \Delta\mathbf{H} = \frac{\partial \mathbf{P}_\parallel}{\partial t} - \hat{\mathbf{z}} \times \nabla_\parallel M_z \tag{3a}$$

$$\hat{\mathbf{z}} \times \Delta\mathbf{E} = -\mu_0 \frac{\partial \mathbf{M}_\parallel}{\partial t} - \hat{\mathbf{z}} \times \nabla_\parallel \left(\frac{P_z}{\epsilon_0}\right), \tag{3b}$$

where $\mathbf{E} = [E_x,\ E_y,\ E_z]^{\mathrm{T}}$ and $\mathbf{H} = [H_x,\ H_y,\ H_z]^{\mathrm{T}}$ are the fields interacting with the surface, $\mathbf{P} = [P_x,\ P_y,\ P_z]^{\mathrm{T}}$ and $\mathbf{M} = [M_x,\ M_y,\ M_z]^{\mathrm{T}}$ are the surface electric and magnetic polarizations, and $\Delta\psi = \psi_t - \psi_i - \psi_r$ is the difference operator with $\psi \in \{E, H\}$ and $\{i, t, r\}$ corresponding to the incident, reflect and transmitted field at the surface, respectively. Evaluation of (3), leads to

$$\begin{bmatrix} -\Delta H_y \\ \Delta H_x \end{bmatrix} = \begin{bmatrix} \frac{\partial P_x}{\partial t} + \frac{\partial M_z}{\partial y} \\ \frac{\partial P_y}{\partial t} - \frac{\partial M_z}{\partial x} \end{bmatrix} \tag{4a}$$

$$\begin{bmatrix} -\Delta E_y \\ \Delta E_x \end{bmatrix} = \begin{bmatrix} -\mu_0 \frac{\partial M_x}{\partial t} + \frac{\partial}{\partial y}\left(\frac{P_z}{\epsilon_0}\right) \\ -\mu_0 \frac{\partial M_y}{\partial t} - \frac{\partial}{\partial x}\left(\frac{P_z}{\epsilon_0}\right) \end{bmatrix}, \tag{4b}$$

which represents the GSTCs in the time domain, relating the difference in the transverse fields with time-derivatives of the

tangential surface polarization and transverse spatial derivatives of the normal components of the surface polarizations. Moreover, the surface polarization terms at the surface for a non-local, temporally and spatially dispersive response can be related to the average fields on the surface using the following convolutional constitutive relations [1],

$$\mathbf{P} = \epsilon_0 \overline{\overline{\chi}}_{\mathrm{ee}} * \mathbf{E}_{\mathrm{av}} + \frac{1}{c_0} \overline{\overline{\chi}}_{\mathrm{em}} * \mathbf{H}_{\mathrm{av}}$$
$$\mathbf{M} = \overline{\overline{\chi}}_{\mathrm{mm}} * \mathbf{H}_{\mathrm{av}} + \frac{1}{\eta_0} \overline{\overline{\chi}}_{\mathrm{me}} * \mathbf{E}_{\mathrm{av}},$$

where $\psi_{\mathrm{av}} = (\psi_i + \psi_r + \psi_t)/2$ is the average fields on the surface and $\overline{\overline{\chi}}_{ab}$ with $\{a, b\} \in (e, m)$ correspond to the surface susceptibility tensors,

$$\overline{\overline{\chi}}_{\mathrm{ee}} = \begin{pmatrix} \chi_{\mathrm{ee}}^{xx} & \chi_{\mathrm{ee}}^{xy} & \chi_{\mathrm{ee}}^{xz} \\ \chi_{\mathrm{ee}}^{yx} & \chi_{\mathrm{ee}}^{yy} & \chi_{\mathrm{ee}}^{yz} \\ \chi_{\mathrm{ee}}^{zx} & \chi_{\mathrm{ee}}^{zy} & \chi_{\mathrm{ee}}^{zz} \end{pmatrix},$$
$$\overline{\overline{\chi}}_{\mathrm{em}} = \begin{pmatrix} \chi_{\mathrm{em}}^{xx} & \chi_{\mathrm{em}}^{xy} & \chi_{\mathrm{em}}^{xz} \\ \chi_{\mathrm{em}}^{yx} & \chi_{\mathrm{em}}^{yy} & \chi_{\mathrm{em}}^{yz} \\ \chi_{\mathrm{em}}^{zx} & \chi_{\mathrm{em}}^{zy} & \chi_{\mathrm{em}}^{zz} \end{pmatrix}$$
$$\overline{\overline{\chi}}_{\mathrm{mm}} = \begin{pmatrix} \chi_{\mathrm{mm}}^{xx} & \chi_{\mathrm{mm}}^{xy} & \chi_{\mathrm{mm}}^{xz} \\ \chi_{\mathrm{mm}}^{yx} & \chi_{\mathrm{mm}}^{yy} & \chi_{\mathrm{mm}}^{yz} \\ \chi_{\mathrm{mm}}^{zx} & \chi_{\mathrm{mm}}^{zy} & \chi_{\mathrm{mm}}^{zz} \end{pmatrix},$$
$$\overline{\overline{\chi}}_{\mathrm{me}} = \begin{pmatrix} \chi_{\mathrm{me}}^{xx} & \chi_{\mathrm{me}}^{xy} & \chi_{\mathrm{me}}^{xz} \\ \chi_{\mathrm{me}}^{yx} & \chi_{\mathrm{me}}^{yy} & \chi_{\mathrm{em}}^{yz} \\ \chi_{\mathrm{me}}^{zx} & \chi_{\mathrm{me}}^{zy} & \chi_{\mathrm{me}}^{zz} \end{pmatrix}.$$

For simplicity and without loss of generality in the upcoming derivations and methods, we are going to consider the case of a monoanistropic surface with no normal components under TE excitation. Therefore, simplifying the GSTCs and constitutive relations to the following

$$\Delta E_y = \mu_0 \frac{\partial M_x}{\partial t}, \quad M_x = \chi_{\mathrm{mm}}^{xx} * H_{x,\mathrm{av}}$$
$$\Delta H_x = \frac{\partial P_y}{\partial t}, \quad P_y = \epsilon_0 \chi_{\mathrm{ee}}^{yy} * E_{y,\mathrm{av}}.$$

Consider now that this zero-thickness surface is placed between nodes k_s and $k_s + 1$ in the Yee-cell, as shown in Fig. 1(c). Following the tight-asymmetric (TA) cell scheme in [12], virtual surface nodes, $E_y|_{i,s^-}$, $H_x|_{i,s^+}$ and $H_z|_{i,s^-}$ are inserted right before and after the surface so that Maxwell's curl equations can be evaluated for bulk field nodes interacting with the surface field nodes. Following this discretization scheme, difference and average fields are defined as

$$\Delta E_y \to E_y|_{i,k_s+1} - E_y|_{i,s^-}$$
$$\Delta H_y \to H_x|_{i,s^+} - H_x|_{i,k_s}$$
$$E_{y,\mathrm{av}} \to \frac{E_y|_{i,k_s+1} + E_y|_{i,s^-}}{2}$$
$$H_{x,\mathrm{av}} \to \frac{H_x|_{i,s^+} + H_x|_{i,k_s}}{2}.$$

For the case of a monoanisotropic metasurface, under TE oblique incidence, the tangential electric and magnetic susceptibilities can be obtained from full-wave simulation according to [25],

$$\tilde{\chi}_{\mathrm{ee}}(k_x = k_0 \sin\theta) = \frac{2j\cos\theta}{k_0} \left(\frac{\mathcal{R} + \mathcal{T} - 1}{\mathcal{T} + \mathcal{R} + 1} \right) \tag{5a}$$
$$\tilde{\chi}_{\mathrm{mm}}(k_x = k_0 \sin\theta) = \frac{2j}{k_0 \cos\theta} \left(\frac{\mathcal{R} - \mathcal{T} + 1}{\mathcal{R} - \mathcal{T} - 1} \right). \tag{5b}$$

where k_0 is the free space wavenumber and $\mathcal{R}$ and $\mathcal{T}$ are the reflection and transmission coefficients for a given frequency and angle of incidence. From (5), we can obtain the reflection and transmission as a function of the susceptibilities according to,

$$\mathcal{R} = \frac{2jk_0\{\cos\theta^2 \chi_{\mathrm{mm}}^{xx} - \chi_{\mathrm{ee}}^{yy}\}}{\{jk_0 \chi_{\mathrm{ee}}^{yy} + 2\cos\theta\}\{jk_0 \cos\theta \chi_{\mathrm{mm}}^{xx} + 2\}} \tag{6a}$$
$$\mathcal{T} = \frac{\cos\theta[4 + k_0^2 \chi_{\mathrm{mm}}^{xx} \chi_{\mathrm{ee}}^{yy}]}{\{jk_0 \chi_{\mathrm{ee}}^{yy} + 2\cos\theta\}\{jk_0 \cos\theta \chi_{\mathrm{mm}}^{xx} + 2\}}. \tag{6b}$$

Thus, completing the set of equations that form the background required for constructing temporal and spatial dispersion in the GSTC-FDTD methods in the subsequent sections.

IV. LORENTZIAN TEMPORAL AND SPATIAL DISPERSION METHOD (GSTC-FDTD-TDSD)

A. METHOD FORMULATION

Let us start with the implicit method in the time and space domain, referred to in this work as GSTC-FDTD-TDSD. The polarization at the metasurface can be described as a summation of polarization components based on the susceptibilities excited. For instance, the tangential P_y and M_x components can be described as

$$P_y = P_{\mathrm{ee}}^{yx} + P_{\mathrm{ee}}^{yy} + P_{\mathrm{ee}}^{yz} + P_{\mathrm{em}}^{yx} + P_{\mathrm{em}}^{yy} + P_{\mathrm{em}}^{yz}$$
$$M_x = M_{\mathrm{mm}}^{xx} + M_{\mathrm{mm}}^{xy} + M_{\mathrm{mm}}^{xz} + M_{\mathrm{me}}^{xx} + M_{\mathrm{me}}^{xy} + M_{\mathrm{me}}^{xz}.$$

Time and spatial dispersion can be incorporated for each one of these terms using the extended Lorentz model [1],

$$\frac{\partial^2 \mathcal{P}_{\mathrm{ee}}^{yy}}{\partial t^2} + \gamma(k_x) \frac{\partial \mathcal{P}_{\mathrm{ee}}^{yy}}{\partial t} + \omega_0^2(k_x) \mathcal{P}_{\mathrm{ee}}^{yy} = \epsilon_0 \omega_p^2(k_x) \mathcal{E}_{y,\mathrm{av}}, \tag{7}$$

where k_x is the transverse wavenumber and

$$\gamma = \alpha_0 + \alpha_1 k_x + \alpha_2 k_x^2 + O(k_x^n) \tag{8a}$$
$$\omega_p^2 = \beta_0^2 + \beta_1 k_x + \beta_2 k_x^2 + O(k_x^n) \tag{8b}$$
$$\omega_0^2 = \zeta_0^2 + \zeta_1 k_x + \zeta_2 k_x^2 + O(k_x^n), \tag{8c}$$

is the polynomial expansion of the Lorentz parameters in the spatial frequency domain, referred to as the extended Lorentz parameters.

Let us now consider the uniform monoanisotropic TE case with only tangential electric and magnetic polarization terms P_{ee}^{yy} and M_{mm}^{xx} described by tangential electric and magnetic susceptibilities χ_{ee}^{yy} and χ_{mm}^{xx}, respectively. For a compact notation, let us write $P_{\mathrm{ee}}^{yy} \to P_y$ and $M_{\mathrm{mm}}^{xx} \to M_x$.

Assuming without loss of generality, a symmetric spatial response in (8) (even powers of k_x) for terms up to second-order. We obtain for the description of an extended Lorentz

oscillator model associated with, for example, the electric polarization in the time and space domain as,

$$\frac{\partial^2 P_y}{\partial t^2} + \left(\alpha_{0,e} - \alpha_{2,e}\frac{\partial^2}{\partial x^2}\right)\frac{\partial P_y}{\partial t} + \left(\zeta_{0,e}^2 - \zeta_{2,e}\frac{\partial^2}{\partial x^2}\right)P_y = \epsilon_0\left(\beta_{0,e}^2 - \beta_{2,e}\frac{\partial^2}{\partial x^2}\right)E_{y,\mathrm{av}}. \tag{9}$$

where the second subscript "e" on the Lorentz parameters specifies values associated with the electric polarization.

Next, for improved numerical accuracy let us consider first-order time and space derivatives only, by adding auxiliary differential equations (ADEs). Considering the tight-asymmetric (TA) cell with the TE GSTCs and tangential susceptibility only, the resulting system of equations is then comprised of: 1) a set of equations describing the electric polarization from (9) using a first order construction,

$$\frac{\partial P_y^{t'}}{\partial t} + \alpha_{0,e}P_y^{t'} - \alpha_{2,e}\frac{\partial}{\partial x}P_y^{t'x'} + \zeta_{0,e}^2 P_y - \zeta_{2,e}\frac{\partial}{\partial x}P_y^{x'} = \epsilon_0\left(\beta_{0,e}^2 E_{y,\mathrm{av}} - \beta_{2,e}\frac{\partial}{\partial x}E_{y,\mathrm{av}}^{x'}\right), \tag{10a}$$

$$P_y^{t'} - \frac{\partial P_y}{\partial t} = 0, \quad P_y^{t'x'} - \frac{\partial P_y^{t'}}{\partial x} = 0 \tag{10b}$$

$$P_y^{x'} - \frac{\partial P_y}{\partial x} = 0, \quad E_{y,\mathrm{av}}^{x'} - \frac{\partial E_{y,\mathrm{av}}}{\partial x} = 0; \tag{10c}$$

2) a complimentary set of equations for the magnetic polarization,

$$\frac{\partial M_x^{t'}}{\partial t} + \alpha_{0,m}M_x^{t'} - \alpha_{2,m}\frac{\partial}{\partial x}M_x^{t'x'} + \zeta_{0,m}^2 M_x - \zeta_{2,m}\frac{\partial}{\partial x}M_x^{x'} = \epsilon_0\left(\beta_{0,m}^2 H_{x,\mathrm{av}} - \beta_{2,m}\frac{\partial}{\partial x}H_{x,\mathrm{av}}^{x'}\right) \tag{10d}$$

$$M_x^{t'} - \frac{\partial M_x}{\partial t} = 0, \quad M_x^{t'x'} - \frac{\partial M_x^{t'}}{\partial x} = 0 \tag{10e}$$

$$M_x^{x'} - \frac{\partial M_x}{\partial x} = 0, \quad H_{x,\mathrm{av}}^{x'} - \frac{\partial H_{x,\mathrm{av}}}{\partial x} = 0; \tag{10f}$$

and, finally, 3) four equations describing the field updates for the special cells and the GSTCs,

$$-\Delta E_y = -\frac{\partial M_x}{\partial t}, \quad \frac{\partial E_y}{\partial t} = \frac{1}{\epsilon_0}\left(\frac{\partial H_x}{\partial z} - \frac{\partial H_z}{\partial x}\right) \tag{10g}$$

$$\Delta H_x = \frac{\partial P_y}{\partial t}, \quad \frac{\partial H_x}{\partial t} = \frac{1}{\mu_0}\frac{\partial E_y}{\partial z}. \tag{10h}$$

One important difference compared to the temporal-dispersive-only case in [12] is that now, due to spatial dispersion, we have to solve a coupled system of equations, where all points along the surface must be solved at the same time self-consistently. A second consideration about the system of equations in (10) is that the number of additional ADEs (unknowns) is equal to $n_d - 1$ for each of the polynomials in (8), where n_d is the highest-order derivative in each of the extended Lorentz terms. In the current example, since all the terms are expanded up to the second order, there are three additional ADEs (variables) for each polarization term.

TABLE 1. Case 1: Custom TDSD Electric Susceptibility Parameters.

Tangential Electric Susceptibility (χ_{ee}^{yy})					
α_0 ($\times 10^6$)	α_2 –	β_0 ($\times 10^{12}$)	β_2 ($\times 10^9$)	ζ_0 ($\times 10^{15}$)	ζ_2 ($\times 10^{15}$)
7.5398	0.7539	0.2126	0.5315	1.5079	12.0637

TABLE 2. Case 2: Custom TDSD Electric and Magnetic Susceptibility Parameters.

Tangential Electric Susceptibility (χ_{ee}^{yy})					
α_0 ($\times 10^{12}$)	α_2 ($\times 10^0$)	β_0 ($\times 10^{11}$)	β_2 ($\times 10^8$)	ζ_0 ($\times 10^{15}$)	ζ_2 ($\times 10^{16}$)
7.5398	75.3982	3.0121	7.5303	1.4451	5.0579
Tangential Magnetic Susceptibility (χ_{mm}^{xx})					
α_0 ($\times 10^{12}$)	α_2 ($\times 10^0$)	β_0 ($\times 10^{11}$)	β_2 ($\times 10^8$)	ζ_0 ($\times 10^{15}$)	ζ_2 ($\times 10^{16}$)
7.5398	75.3982	3.0121	7.5303	1.4451	5.0579

Discretizing (10) using Forward-Euler for time derivatives and spatial Forward-Euler for E and P and spatial Backward-Euler for H and M terms results in the system of equations (S1) in Supplementary Material S1. Equation (S1) is defined for a given cell i along the surface, where boxed terms correspond to unknowns to be determined and are summarized in the following $\mathbb{X}$ vector

$$\mathbb{X}|_i^{n+1} = \Big[E_y|_{i,k_s+1}^{n+1} \quad E_y|_{i,s^-}^{n+1} \quad H_x|_{i,s^+}^{n+\frac{1}{2}} \quad H_x|_{i,k_s}^{n+\frac{1}{2}} \quad P_y^{t'}|_i^{n+1} \quad P_y|_i^{n+1} \quad P_y^{t'x'}|_i^{n+1} \quad P_y^{x'}|_i^{n+1} \quad E_{y,\mathrm{av}}^{x'}|_i^{n+1} \quad M_x^{t'}|_i^{n+\frac{1}{2}} \quad M_x|_i^{n+\frac{1}{2}} \quad M_x^{t'x'}|_i^{n+\frac{1}{2}} \quad M_x^{x'}|_i^{n+\frac{1}{2}} \quad H_{x,\mathrm{av}}^{x'}|_i^{n+\frac{1}{2}}\Big]^{\mathrm{T}}. \tag{11}$$

Moreover, for each cell, the complete set of equations, considering the spatial coupling due to spatial dispersion, is represented as

$$\begin{bmatrix}\mathbb{A}|_{i,i-1}^{n+1} & \mathbb{A}|_i^{n+1} & \mathbb{A}|_{i,i+1}^{n+1}\end{bmatrix}\begin{bmatrix}\mathbb{X}|_{i-1}^{n+1}\\ \mathbb{X}|_i^{n+1}\\ \mathbb{X}|_{i+1}^{n+1}\end{bmatrix} = \begin{bmatrix}\mathbb{B}|_{i,i-1}^{n} & \mathbb{B}|_i^{n} & \mathbb{B}|_{i,i+1}^{n}\end{bmatrix}\begin{bmatrix}\mathbb{X}|_{i-1}^{n}\\ \mathbb{X}|_i^{n}\\ \mathbb{X}|_{i+1}^{n}\end{bmatrix} + \mathbb{C}|_i^n, \tag{12}$$

where $\mathbb{A}$ are the coefficient matrices, $\mathbb{B}$ are the forcing term matrices that depend on past values of the unknowns in $\mathbb{X}$, and $\mathbb{C}$ matrices are forcing terms that depend on field terms not part of the unknowns. Each entry within these matrices is presented in Supplementary Material S2 in equations (S2-S8).

After these matrices have been computed for every point on the surface, they need to be assembled in the coupled system of equations for a consistent solution. The final coupled system of equations takes the matrix form shown in (14), bottom of page 7, assuming periodic boundary

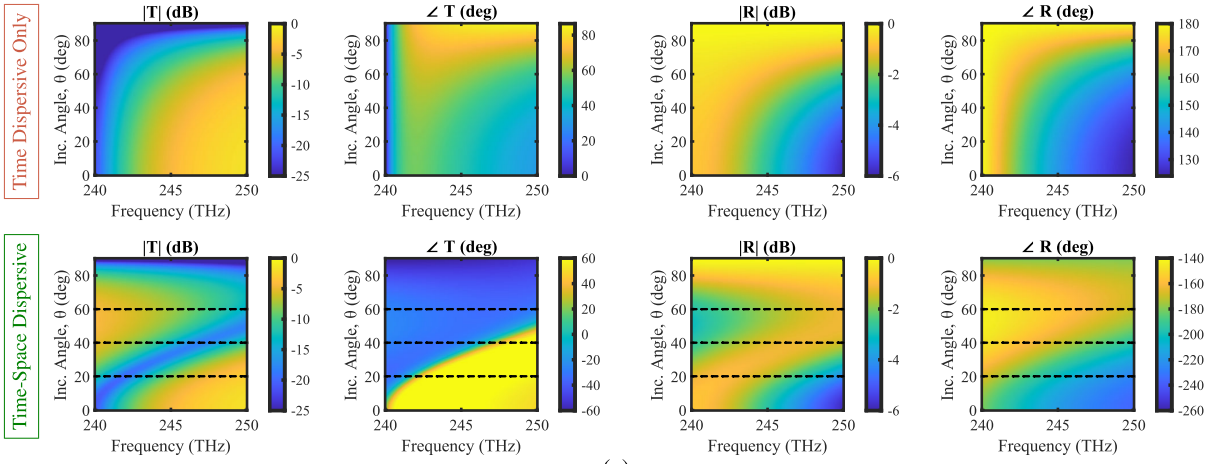

(a)

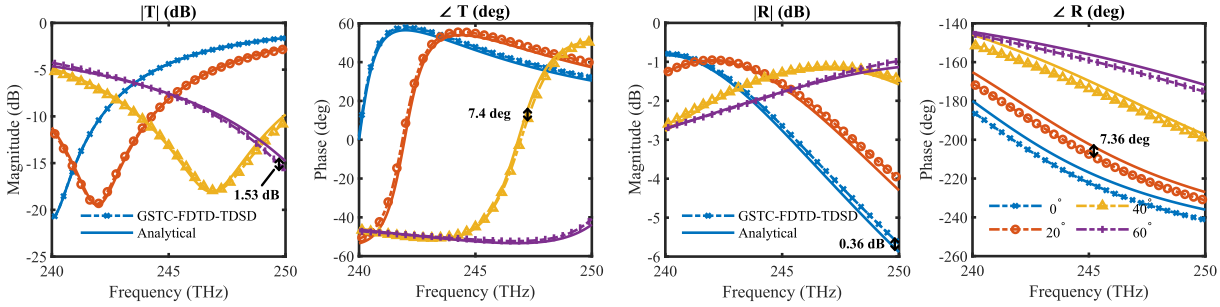

(b)

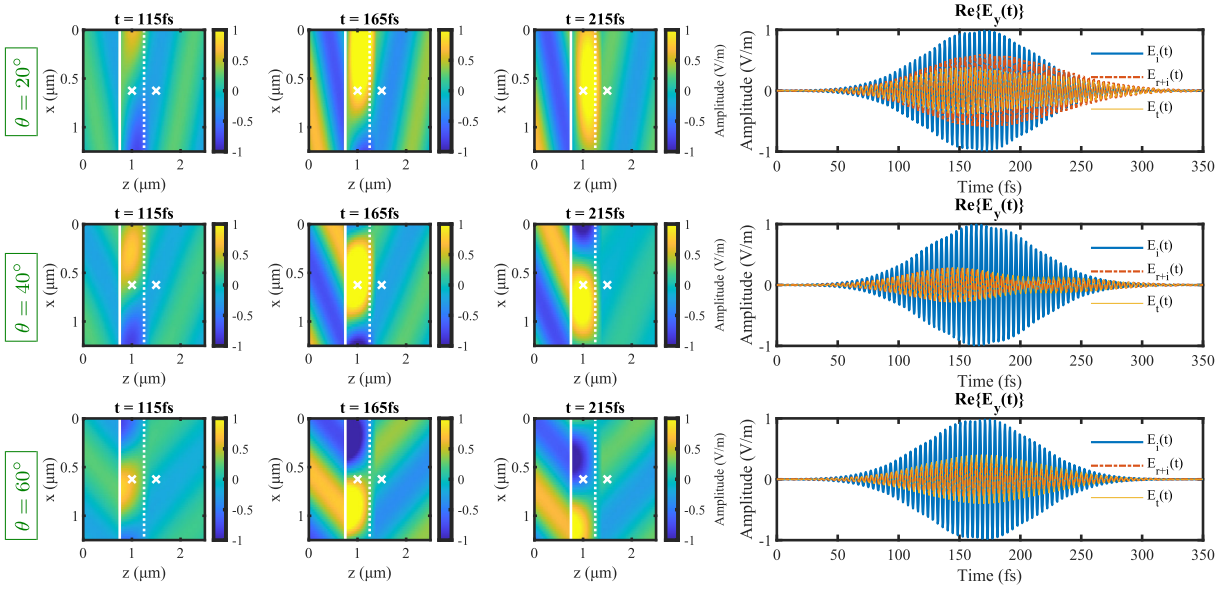

(c)

FIGURE 2. (a) Analytical comparison of transmission and reflection magnitudes (dB) and phases (deg) for a uniform metasurface made of a custom electric susceptibility function defined by the parameters in Tab 1. The top panels show the analytical data for time dispersive susceptibility ($\chi(\omega)$), and the bottom panels show data for a time and space dispersive scenario ($\chi(\omega, k_x)$). (b) Transmission and reflection where solid lines are analytical data obtained from (6), and marked dot-dashed lines are the results obtained from the GSTC-FDTD-TDSD algorithm. Line markers denote the angle of incidence. Arrow insets show the maximum absolute error. (c) The amplitude of the real part of the electric field over time. Image panels show field snapshots over the simulation region for three different angles of incidence and three different time instants. The insets show the source plane location (white solid line), the metasurface location (white dashed line), and the location of the reflection and transmission point monitors (white 'x' markers).

conditions at the end of the surface along the x-direction, with special attention to $\mathbb{C}|_1^n$ and $\mathbb{C}|_{n_x+1}^n$ regarding the periodic boundary conditions, as shown in Eq. (13), bottom of the next page.

The solution at each time step $n\Delta t$ is obtained through the following steps:

1) Update bulk H nodes using regular Yee-cell update equations;
2) Solve for the unknowns in (14);
3) Update the remaining bulk E nodes using regular Yee cell update equations.

B. NUMERICAL DEMONSTRATIONS

For testing the proposed method, we present two simulation cases inside the simulation setup of Fig. 1(a). The first one consists of a single tangential TDSD electric susceptibility case with no magnetic response, and the second case is that of both electric and magnetic surface susceptibility in a Huygens' configuration. For simplicity, these choices of susceptibilities attempt to approximate a single dipole dispersive cell and a Huygens structure that, as shown in [1], may require terms up to the sixth-order in $k_\parallel$. A more practical scenario will be presented in Sec. V with a more robust implementation of the GSTC-FDTD method that easily supports higher-order terms.

The extended Lorentz parameters for the first case are presented in Tab. 1, consisting of terms up to the second-order in the polynomial representation of (8).

The simulation setup consists of a 2.5×2.5 μm region with the metasurface placed at $z = 1.25$ μm. The region is terminated with CPMLs along the z direction and PBCs along the x direction. Simulation parameters are: $\Delta x = \Delta z = 12.5$ nm ($\lambda_0/98$), $\Delta t = 14.74$ as (Courant stability factor of 1/2) running for a total of 700 fs. The source is a Gaussian pulsed plane wave, centered at 245 THz, with a bandwidth of 10 THz and angle of incidence varying from 0° to 60°, and placed at $z = 0.75$ μm. The angle is limited to up to 60° to avoid disturbances caused by the constant phase shift imposed by the PBCs. The reflected and transmitted fields are measured at $2\Delta z$ away from the source, in free space, within bulk Yee-cells, and their spectrum is de-embedded to the face of the metasurface. Time monitors in the reflection region measure both incident and reflected fields.

Results for Case 1 are shown in Fig. 2. Figure 2 (a) shows two rows of panels representing analytical transmission and reflection data for a case of time dispersion only (top row), where the susceptibility is taken to be constant ($k_x = 0$) across different angles of incidence (θ) and a second case, with time and space dispersion (TDSD), where now the electric susceptibility is varying according to the coefficients shown in 1. It is clear that for this custom case, SD becomes important for the correct description of T and R. Moreover, Fig. 2 (b) compares the results of the GSTC-FDTD-TDSD method with analytical analytical results obtained from (6). One of the clear characteristics is the location of the deep minimum in transmission shifting from 240 THz to 250 THz as ζ_2 up-shifts the location of the Lorentz resonance as the angle of incidence increases. Insets show maximum absolute errors of 1.53 dB and 7.4° for magnitude and phase, respectively. Figure 2(c) shows snapshots of the real part of the electric field for different angles of incidence over the simulation region, and the corresponding temporal waveforms in the transmission and reflection regions, showing strong temporal distortion and broadening.

$$\mathbb{C}|_1^n = \begin{bmatrix} \mathbf{0}_{2\times 1} \\ \dfrac{H_x|^{n+\frac{1}{2}}_{1,k_s+1}}{0.75\epsilon_0\Delta z} - \dfrac{H_z|^{n+\frac{1}{2}}_{1,k_s+1} - H_z|^{n+\frac{1}{2}}_{n_x,k_s+1} e^{jk_x\Lambda_x}}{-\epsilon_0\Delta x} \\ \dfrac{-E_y|^n_{1,k_s}}{0.75\mu_0\Delta z} \\ \mathbf{0}_{10\times 1} \end{bmatrix} \text{ and } \mathbb{C}|_{n_x+1}^n = \begin{bmatrix} \mathbf{0}_{2\times 1} \\ \dfrac{H_x|^{n+\frac{1}{2}}_{n_x+1,k_s+1}}{0.75\epsilon_0\Delta z} - \dfrac{H_z|^{n+\frac{1}{2}}_{1,k_s+1} e^{jk_x\Lambda_x} - H_z|^{n+\frac{1}{2}}_{n_x,k_s+1}}{-\epsilon_0\Delta x} \\ \dfrac{-E_y|^n_{n_x+1,k_s}}{0.75\mu_0\Delta z} \\ \mathbf{0}_{10\times 1} \end{bmatrix} \tag{13}$$

$$\begin{bmatrix} \mathbb{A}|_1^{n+1} & \mathbb{A}|_{1,2}^{n+1} & 0 & \cdots & 0 & 0 & 0 \\ 0 & \mathbb{A}|_2^{n+1} & \mathbb{A}|_{2,3}^{n+1} & \cdots & 0 & 0 & 0 \\ \vdots & \vdots & \vdots & \ddots & \vdots & \vdots & \vdots \\ 0 & 0 & 0 & \cdots & 0 & \mathbb{A}|_{n_x}^{n+1} & \mathbb{A}|_{n_x,n_x+1}^{n+1} \\ \mathbb{A}|_{n_x+1,1}^{n+1} e^{-jk_x\Lambda_x} & 0 & 0 & \cdots & 0 & 0 & \mathbb{A}|_{n_x+1}^{n+1} \end{bmatrix} \begin{bmatrix} \mathbb{X}|_1^{n+1} \\ \mathbb{X}|_2^{n+1} \\ \vdots \\ \mathbb{X}|_{n_x}^{n+1} \\ \mathbb{X}|_{n_x+1}^{n+1} \end{bmatrix}$$
$$= \begin{bmatrix} \mathbb{B}|_1^n & \mathbb{B}|_{1,2}^n & 0 & \cdots & 0 & 0 & 0 \\ 0 & \mathbb{B}|_2^n & \mathbb{B}|_{2,3}^n & \cdots & 0 & 0 & 0 \\ \vdots & \vdots & \vdots & \ddots & \vdots & \vdots & \vdots \\ 0 & 0 & 0 & \cdots & 0 & \mathbb{B}|_{n_x}^n & \mathbb{B}|_{n_x,n_x+1}^n \\ \mathbb{B}|_{n_x+1,1}^n e^{-jk_x\Lambda_x} & 0 & 0 & \cdots & 0 & \mathbb{B}|_{n_x+1,n_x}^n & \mathbb{B}|_{n_x+1}^n \end{bmatrix} \begin{bmatrix} \mathbb{X}|_1^n \\ \mathbb{X}|_2^n \\ \vdots \\ \mathbb{X}|_{n_x}^n \\ \mathbb{X}|_{n_x+1}^n \end{bmatrix} + \begin{bmatrix} \mathbb{C}|_1^n \\ \mathbb{C}|_2^n \\ \vdots \\ \mathbb{C}|_{n_x}^n \\ \mathbb{C}|_{n_x+1}^n \end{bmatrix} \tag{14}$$

Case 2 consists of a case where both tangential TDSD electric and magnetic susceptibility parameters are equal at all angles, resembling a Huygens cell characterized by co-located orthogonal electric and magnetic resonance responses [7], [26], [27]. The parameters are presented in Tab. 2. The simulation setup is the same as that of Case 1, and results are shown in Fig. 3. Figure 3(a) shows the comparison between constant susceptibilities across angles of incidence in the top row and their SD counterpart in the bottom row. The effects of SD are clearly depicted by the huge differences in the T and R profiles compared to the time-dispersive-only case. In Fig. 3(b), we observe a good match between the GSTC-FDTD-TDSD method and the analytical results from (6) for various incidence angles. Insets show maximum absolute errors of 1.6 dB and 17° for magnitude and phase, respectively, closer to the edges of the characterization bandwidth. In this case, the surface becomes more transmissive (or better matched) at oblique angles due to optimum interactions of collocated electric and magnetic resonances. However, the response still presents a spatially dispersive profile controlled by the higher-order terms in k_x and manifesting as variation with the angle of incidence. This phenomenon is also depicted in the field plots over time and angle of Fig. 3(c), where the transmitted fields present a lower amplitude at 20° compared to higher angles. These two examples thus successfully illustrate the proposed GSTC-FDTD platform with TD-SD incorporated, along with the importance of including SD in the analysis compared to a purely non-SD case.

So far, the cases analyzed were limited to second-order terms in k_x, which produces second-order derivatives in (9). General metasurface unit cells may require higher order dependence of surface susceptibilities on the incidence angles or equivalently on k_x. In those cases, a need for higher-order terms would require the extension of the system of coupled equations. This is a main drawback of this method; if higher-order terms are required, the whole system of equations becomes larger, new ADEs must be added, and the condition of the matrix $\mathbb{A}$ in (14) (a measurement of how sensitive the matrix is to changes in the input data and roundoff errors in the solution process [28]), increases by several orders of magnitude, even after performing matrix scaling and permutation [29], [30]. This can lead to close to singular matrices or even cases where solutions might diverge. As an approach to solve this limitation and make the method easier to expand for higher-order terms in k_x, in the next section, we propose a Mixed GSTC-FDTD-TDSD that solves (10) in the spatial frequency domain at each time-step.

V. MIXED FINITE-DIFFERENCES SPATIAL-FREQUENCY/TIME-DOMAIN METHOD

As mentioned in the previous section, for the solution of (10) for higher-order terms in k_x and even larger surfaces, it was observed that $\mathbb{A}$ in (14) can become badly conditioned, making the solution unstable, and very sensitive to small changes in the Lorentz parameters and roundoff errors during the solution process. As an attempt to improve these issues, we present in this section a mixed finite differences spatial-frequency/time-domain method (Mixed GSTC-FDTD-TDSD) that solves the surface equations (10) in the spatial frequency domain at every time step.

We start by converting (10) to the spatial frequency domain using the spatial Fourier transform along the surface direction (i.e., x dimension). The spatial derivatives are no longer needed explicitly as they can be replaced in the spatial frequency domain by a k_x factor. We thus obtain a reduced set of equations defining the polarizations,

$$\begin{aligned}
&\frac{\partial \mathcal{M}_x'}{\partial t} + \gamma_m(k_x)\mathcal{M}_x' + \omega_{0,m}^2(k_x)\mathcal{M}_x \\
&\qquad = \mu_0\omega_{p,m}^2(k_x)\mathcal{H}_{x,\mathrm{av}} \\
&\frac{\partial \mathcal{P}_y'}{\partial t} + \gamma_e(k_x)\mathcal{P}_y' + \omega_{0,e}^2(k_x)\mathcal{P}_y \\
&\qquad = \epsilon_0\omega_{p,e}^2(k_x)\mathcal{E}_{y,\mathrm{av}} \\
&\mathcal{P}_y' - \frac{\partial P_y}{\partial t} = 0, \quad \mathcal{M}_x' - \frac{\partial M_x}{\partial t} = 0,
\end{aligned} \tag{15a}$$

and the GSTCs and surface fields,

$$\begin{aligned}
-\Delta\mathcal{E}_y &= -\frac{\partial \mathcal{M}_x}{\partial t}, \quad \frac{\partial \mathcal{E}_y}{\partial t} = \frac{1}{\epsilon_0}\left(\frac{\partial \mathcal{H}_x}{\partial z} - jk_x\mathcal{H}_z\right) \\
\Delta\mathcal{H}_x &= \frac{\partial \mathcal{P}_y}{\partial t}, \quad \frac{\partial \mathcal{H}_x}{\partial t} = \frac{1}{\mu_0}\frac{\partial \mathcal{E}_y}{\partial z},
\end{aligned} \tag{15b}$$

where calligraphic quantities correspond to the spatial frequency representatives of their spatial field counterparts (i.e., $E \rightarrow \mathcal{E}$). Equation (16), as shown at the bottom of page 10, is the discretized version of (15) using FE for time derivatives, BE for z-space derivatives on $\mathcal{H}_x$ and FE for z-space derivatives on $\mathcal{E}_y$.

The physical cells in [1] contain constant electric polarization terms, $P_{y,0}$ and $M_{x,0}$ that are independent of the Lorentz oscillator model and can be added using superposition to the total polarization terms, P_y and M_x,

$$\begin{aligned}
P_y &= P_{y,\mathrm{L}} + P_{y,0} \\
M_x &= M_{x,\mathrm{L}} + M_{x,0}.
\end{aligned}$$

The two non-dispersive terms are then related to the average fields on the surface using standard constitutive relations,

$$\begin{aligned}
\mathcal{P}_{y,0} &= \epsilon_0\chi_{\mathrm{ee},0}^{yy}\mathcal{E}_{y,\mathrm{av}} \\
\mathcal{M}_{x,0} &= \mu_0\chi_{\mathrm{mm},0}^{xx}\mathcal{H}_{x,\mathrm{av}},
\end{aligned}$$

which conforms to the following discretized scheme:

$$\begin{aligned}
\boxed{\mathcal{P}_{y,0}|_i^{n+1}} &= \epsilon_0\chi_{\mathrm{ee},0}^{yy}\frac{\boxed{\mathcal{E}_y|_{i,k_s+1}^{n+1}} + \boxed{\mathcal{E}_y|_{i,s^-}^{n+1}}}{2} \\
\boxed{\mathcal{M}_{x,0}|_i^{n+\frac{1}{2}}} &= \mu_0\chi_{\mathrm{mm},0}^{xx}\frac{\boxed{\mathcal{H}_x|_{i,s^+}^{n+\frac{1}{2}}} + \boxed{\mathcal{H}_x|_{i,k_s}^{n+\frac{1}{2}}}}{2}.
\end{aligned}$$

It is worth noting that the overall susceptibility description across frequency and all angles of incidence must still follow Kramers-Kronig relations for a stable causal response. Furthermore, we can incorporate all these equations in and

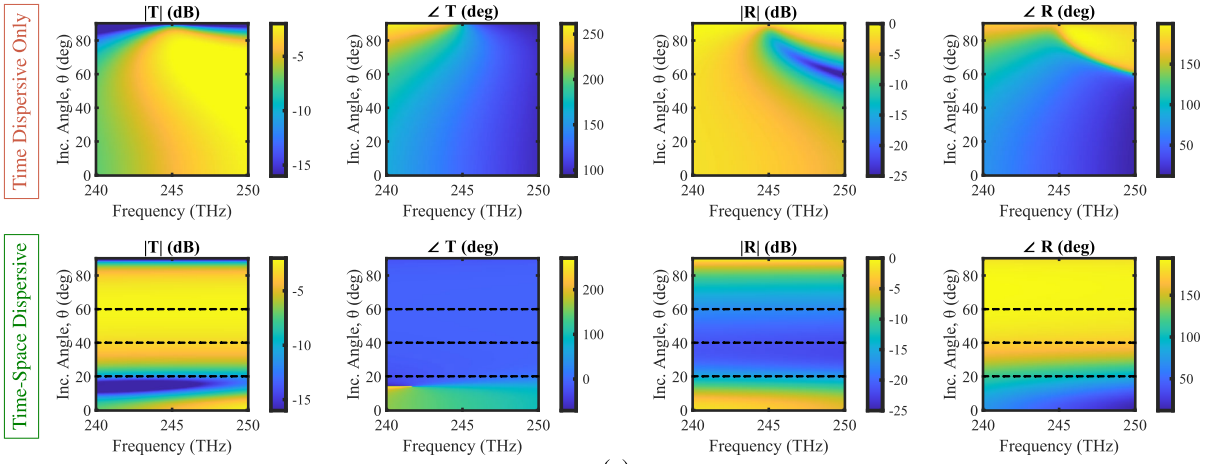

(a)

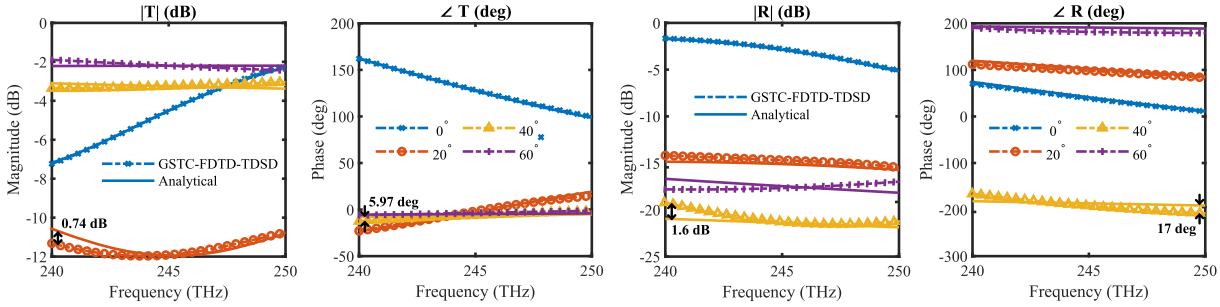

(b)

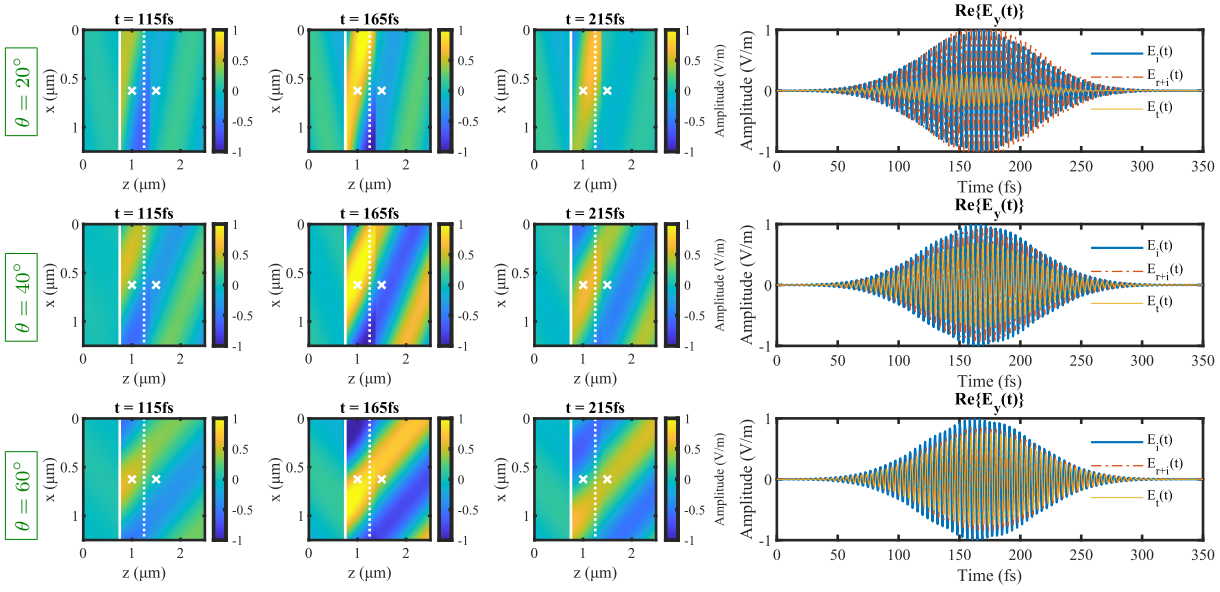

(c)

FIGURE 3. (a) Analytical comparison of transmission and reflection magnitudes (dB) and phases (deg) for a uniform metasurface made of custom electric and magnetic susceptibility functions defined by the parameters in Tab 2. The top panels show the analytical data for time dispersive susceptibilities ($\chi(\omega)$), and the bottom panels show data for a time and space dispersive scenario ($\chi(\omega, k_x)$). (b) Transmission and reflection where solid lines are analytical data obtained from (6), and marked dot-dashed lines are the results obtained from the GSTC-FDTD-TDSD algorithm. Line markers denote the angle of incidence. Arrow insets show the maximum absolute error. (c) The amplitude of the real part of the electric field over time. Image panels show field snapshots over the simulation region for three different angles of incidence and three different time instants. The insets show the source plane location (white solid line), the metasurface location (white dashed line), and the location of the reflection and transmission point monitors (white 'x' markers).

write their final matrix form as shown in (17), bottom of the next page.

It is worth mentioning that in this particular system of equations, the index i refers to the discrete values of $k_{x,i}$ in

the spatial frequency domain, defined as

$$k_x = \left[\cdots k_{x,i} \cdots\right] = 2\pi\left[-\frac{1}{2dx} \cdots \frac{1/dx-1/2}{n_{x,\mathrm{MS}}-1} \cdots \frac{1}{2dx} - \frac{1}{2}\right], \tag{18}$$

where $n_{x,\mathrm{MS}}$ is the number of sample points along the surface, $1/dx$ is the spatial sampling frequency, and $(1/dx - 1/2)/(n_{x,\mathrm{MS}} - 1)$ is the size of the spatial frequency bin. For a scenario where the surface length and space-step provide a coarse value of $k_{x,i}$, the spatial frequency bins in the k_x domain become large, and spectral leakage occurs. In this

$$\boxed{\mathcal{E}_y|_{i,k_s+1}^{n+1}} - \boxed{\mathcal{E}_y|_{i,s^-}^{n+1}} = \frac{\boxed{\mathcal{M}_x|_i^{n+\frac{1}{2}}} - \mathcal{M}_x|_i^{n-\frac{1}{2}}}{\Delta t}, \quad \boxed{\mathcal{H}_x|_{i,s^+}^{n+\frac{1}{2}}} - \boxed{\mathcal{H}_x|_{i,k_s}^{n+\frac{1}{2}}} = \frac{\boxed{\mathcal{P}_y|_i^{n+1}} - \mathcal{P}_y|_i^n}{\Delta t}$$

$$\frac{\boxed{\mathcal{E}_y|_{i,k_s+1}^{n+1}} - \mathcal{E}_y|_{i,k_s+1}^n}{\Delta t} = \frac{\mathcal{H}_x|_{i,k_s+1}^{n+\frac{1}{2}} - \boxed{\mathcal{H}_x|_{i,s^+}^{n+\frac{1}{2}}}}{0.75\epsilon_0\Delta z} - jk_{x,i}\frac{\mathcal{H}_z|_{i,k_s+1}^{n+\frac{1}{2}}}{\epsilon_0}$$

$$\frac{\boxed{\mathcal{H}_x|_{i,k_s}^{n+\frac{1}{2}}} - \mathcal{H}_x|_{i,k_s}^{n-\frac{1}{2}}}{\Delta t} = \frac{\mathcal{E}_y|_{i,s^-}^n - \mathcal{E}_y|_{i,k_s}^n}{0.75\mu_0\Delta z}$$

$$\frac{\boxed{\mathcal{P}'_y|_i^{n+1}} - \mathcal{P}'_y|_i^n}{\Delta t} + \gamma_e\frac{\boxed{\mathcal{P}'_y|_i^{n+1}} + \mathcal{P}'_y|_i^n}{2} + \omega_{0,e}^2\frac{\boxed{\mathcal{P}_y|_i^{n+1}} + \mathcal{P}_y|_i^n}{2} = \epsilon_0\omega_{p,e}^2\frac{\boxed{\mathcal{E}_y|_{i,k_s+1}^{n+1}} + \boxed{\mathcal{E}_y|_{i,s^-}^{n+1}} + \mathcal{E}_y|_{i,k_s+1}^n + \mathcal{E}_y|_{i,s^-}^n}{4}$$

$$\frac{\boxed{\mathcal{M}'_x|_i^{n+\frac{1}{2}}} - \mathcal{M}'_x|_i^{n-\frac{1}{2}}}{\Delta t} + \gamma_e\frac{\boxed{\mathcal{M}'_x|_i^{n+\frac{1}{2}}} + \mathcal{M}'_x|_i^{n-\frac{1}{2}}}{2} + \omega_{0,m}^2\frac{\boxed{\mathcal{M}_x|_i^{n+\frac{1}{2}}} + \mathcal{M}_x|_i^{n-\frac{1}{2}}}{2} = \mu_0\omega_{p,m}^2\frac{\boxed{\mathcal{H}_x|_{i,s^+}^{n+\frac{1}{2}}} + \boxed{\mathcal{H}_x|_{i,k_s}^{n+\frac{1}{2}}} + \mathcal{H}_x|_{i,s^+}^{n-\frac{1}{2}} + \mathcal{H}_x|_{i,k_s}^{n-\frac{1}{2}}}{4}$$

$$-\frac{\boxed{\mathcal{P}'_y|_i^{n+1}} + \mathcal{P}'_y|_i^n}{2} + \frac{\boxed{\mathcal{P}_y|_i^{n+1}} - \mathcal{P}_y|_i^n}{\Delta t} = 0, \quad -\frac{\boxed{\mathcal{M}'_x|_i^{n+\frac{1}{2}}} + \mathcal{M}'_x|_i^{n-\frac{1}{2}}}{2} + \frac{\boxed{\mathcal{M}_x|_i^{n+\frac{1}{2}}} - \mathcal{M}_x|_i^{n-\frac{1}{2}}}{\Delta t} = 0 \tag{16}$$

$$\begin{bmatrix}
\Delta t & -\Delta t & 0 & 0 & 0 & 0 & -1 & 0 & -1 \\
0 & 0 & \Delta t & -\Delta t & -1 & 0 & -1 & 0 & 0 & 0 \\
1 & 0 & \frac{\Delta t}{0.75\epsilon_0\Delta z} & 0 & 0 & 0 & 0 & 0 & 0 & 0 \\
0 & 0 & 0 & 1 & 0 & 0 & 0 & 0 & 0 & 0 \\
-\frac{\epsilon_0\Delta t\omega_{p,e}^2}{4\omega_{0,e}} & -\frac{\epsilon_0\Delta t\omega_{p,e}^2}{4\omega_{0,e}} & 0 & 0 & 0 & \left(1+\frac{\gamma_e\Delta t}{2}\right) & \frac{\omega_{0,e}\Delta t}{2} & 0 & 0 & 0 \\
0 & 0 & 0 & 0 & 0 & -\frac{\omega_{0,e}\Delta t}{2} & 1 & 0 & 0 & 0 \\
0 & 0 & -\frac{\mu_0\Delta t\omega_{p,m}^2}{4\omega_{0,m}} & -\frac{\mu_0\Delta t\omega_{p,m}^2}{4\omega_{0,m}} & 0 & 0 & 0 & 0 & \left(1+\frac{\gamma_m\Delta t}{2}\right) & \frac{\omega_{0,m}\Delta t}{2} \\
0 & 0 & 0 & 0 & 0 & 0 & 0 & 0 & -\frac{\omega_{0,m}\Delta t}{2} & 1 \\
-\frac{\epsilon_0\chi_{\mathrm{ee},0}^{yy}}{2} & -\frac{\epsilon_0\chi_{\mathrm{ee},0}^{yy}}{2} & 0 & 0 & 1 & 0 & 0 & 0 & 0 & 0 \\
0 & 0 & -\frac{\mu_0\chi_{\mathrm{mm},0}^{xx}}{2} & -\frac{\epsilon_0\chi_{\mathrm{ee},0}^{yy}}{2} & 0 & 0 & 0 & 1 & 0 & 0
\end{bmatrix}$$

$$\cdot \begin{bmatrix}
\mathcal{E}_y|_{i,k_s+1}^{n+1} \\ \mathcal{E}_y|_{i,s^-}^{n+1} \\ \mathcal{H}_x|_{i,s^+}^{n+\frac{1}{2}} \\ \mathcal{H}_x|_{i,k_s}^{n+\frac{1}{2}} \\ \mathcal{P}_{y,0}|_i^{n+1} \\ \mathcal{P}'_{y,\mathrm{L}}|_i^{n+1} \\ \mathcal{P}_{y,\mathrm{L}}|_i^{n+1} \\ \mathcal{M}_{x,0}|_i^{n+\frac{1}{2}} \\ \mathcal{M}'_{x,\mathrm{L}}|_i^{n+\frac{1}{2}} \\ \mathcal{M}_{x,\mathrm{L}}|_i^{n+\frac{1}{2}}
\end{bmatrix} = \begin{bmatrix}
-\mathcal{M}_{x,\mathrm{L}}|_i^{n-\frac{1}{2}} \\
-\mathcal{P}_{y,\mathrm{L}}|_i^n \\
\mathcal{E}_y|_{i,k_s+1}^n + \frac{\Delta t}{0.75\epsilon_0\Delta z}\mathcal{H}_x|_{i,k_s+1}^{n+\frac{1}{2}} - \frac{jk_{x,i}\Delta t}{\epsilon_0}\mathcal{H}_z|_{i,k_s+1}^{n+\frac{1}{2}} \\
\mathcal{H}_x|_{i,k_s}^{n-\frac{1}{2}} + \frac{\Delta t}{0.75\mu_0\Delta z}\left(\mathcal{E}_y|_{i,s^-}^n - \mathcal{E}_y|_{i,k_s}^n\right) \\
\left(1-\frac{\gamma_e\Delta t}{2}\right)\mathcal{P}'_{y,\mathrm{L}}|_i^n - \frac{\omega_{0,e}\Delta t}{2}\mathcal{P}_{y,\mathrm{L}}|_i^n + \frac{\epsilon_0\Delta t\omega_{p,e}^2}{4\omega_{0,e}}\left(\mathcal{E}_y|_{i,k_s+1}^n + \mathcal{E}_y|_{i,s^-}^n\right) \\
\frac{\omega_{0,e}\Delta t}{2}\mathcal{P}'_{y,\mathrm{L}}|_i^n + \mathcal{P}_{y,\mathrm{L}}|_i^n \\
\left(1-\frac{\gamma_m\Delta t}{2}\right)\mathcal{M}'_{x,\mathrm{L}}|_i^{n-\frac{1}{2}} - \frac{\omega_{0,m}\Delta t}{2}\mathcal{M}_{x,\mathrm{L}}|_i^{n-\frac{1}{2}} + \frac{\mu_0\Delta t\omega_{p,m}^2}{4\omega_{0,m}}\left(\mathcal{H}_x|_{i,s^+}^{n-\frac{1}{2}} + \mathcal{H}_x|_{i,k_s}^{n-\frac{1}{2}}\right) \\
\frac{\omega_{0,m}\Delta t}{2}\mathcal{M}'_{x,\mathrm{L}}|_i^{n-\frac{1}{2}} + \mathcal{M}_{x,\mathrm{L}}|_i^{n-\frac{1}{2}} \\
0 \\ 0
\end{bmatrix}. \tag{17}$$

TABLE 3. Short Electric Dipole: Lorentz Resonator Properties.

Tangential Electric Susceptibility (χ_{ee}^{zz})					
α_0 ($\times 10^9$)	β_0 ($\times 10^9$)	β_2 ($\times 10^{12}$)	ζ_0 ($\times 10^9$)	ζ_2 ($\times 10^{15}$)	$\chi_{ee_0}^{zz}$ –
2.25	7.593	3.578	378.7	−18.5	0

TABLE 4. Dielectric Puck: Single Lorentz Resonators' Properties.

Tangential Electric Susceptibility (χ_{ee}^{zz})								
α_0 ($\times 10^6$)	α_2 –	β_0 ($\times 10^9$)	β_2 ($\times 10^{12}$)	ζ_0 ($\times 10^9$)	ζ_2 ($\times 10^{15}$)	ζ_4 ($\times 10^6$)	ζ_6 –	$\chi_{ee_0}^{zz}$ ($\times 10^{-3}$)
822	−73.33	3.47	26.8	404.6	0.69	−77.6	−586	2.26
Tangential Magnetic Susceptibility (χ_{mm}^{yy})								
α_0 ($\times 10^6$)	α_2 –	β_0 ($\times 10^9$)	β_2 ($\times 10^{12}$)	ζ_0 ($\times 10^9$)	ζ_2 ($\times 10^{15}$)	ζ_4 ($\times 10^6$)	ζ_6 –	$\chi_{mm_0}^{zz}$ ($\times 10^{-3}$)
913	−54.51	5.34	−5.0	393.85	2.53	−949	–	0.5526

case, spectral power goes to a spectral bin that does not precisely correspond to the k_x value where the field is, in fact, incident, leading to two problems: wrong evaluation of the susceptibility transfer function and leakage of the spectral power to a spatial frequency bin that is outside the propagation range $(-k_0, k_0)$.

A solution adopted in this work is to take advantage of the periodic boundary conditions imposed at the edges of the metasurface and, at each time step, and replicate the whole fields along the surface by N_{FFT} times. Thus, increasing the resolution in the spatial frequency domain, as in (18) the new number of samples becomes $n_{x,\text{MS}} \rightarrow N_{\text{FFT}} n_{x,\text{MS}}$. Therefore, reducing the size of the spatial frequency bins and preventing both problems while overall improving the accuracy of the solution once the resulting fields are converted back to the space domain via the inverse spatial FFT and further used by regular Yee-cell update equations for appropriate field propagation.

Finally, the solution at each time step $n\Delta t$ is obtained with the following steps:

1) Update bulk H nodes using regular Yee-cell update equations;
2) Compute the spatial Fourier transform of $H_x|_{k_s+1}^{n+\frac{1}{2}}$, $E_y|_{k_s+1}^{n}$ and $H_z|_{k_s+1}^{n+\frac{1}{2}}$ after replicating them by N_{FFT} times;
3) Solve for the unknowns in (17) for $-k_0 \leq k_x \leq k_0$;
4) Compute the *inverse* spatial Fourier transform of $\mathcal{H}_x|_{k_s}^{n+\frac{1}{2}}$, $\mathcal{E}_y|_{k_s+1}^{n+1}$;
5) Update the remaining bulk E nodes using regular Yee cell update equations.

The second method, therefore, generalizes the SD response of the surface beyond 2nd order spatial derivatives at the expense of performing Fast Fourier Transforms of the surface fields at each time step.

A. NUMERICAL DEMONSTRATIONS

The Mixed GSTC-FDTD-TDSD method will be validated using analytical transmission and reflection equations from (6). The examples discussed use the surface susceptibilities data extracted from physical cells in [1] for the electric dipole unit cell and the Huygens' unit cell. The overall simulation setup is depicted in Fig. 1(a).

The electric dipole data is shown in Tab. 3 with the non-spatially dispersive magnetic polarization term, χ_{mm}^{xx} modeled with a temporally dispersive Drude model, with $\omega_p = 4.9119 \times 10^9$ rad/s and $\gamma = 0.98 \times 10^9$ rad/s. The frequency ranges from 50 to 65 GHz, and the angle of incidence spans from 0° to 50° in steps of 10°. Again, the angle is limited to up to 50° to avoid disturbances caused by the constant phase shift imposed by the PBCs. Fields are monitored two cells away from the surface, within the regular Yee-cell propagation region, then reflection and transmission coefficients are calculated and dembedded to the faces of the zero-thickness surface. The simulation region spans over a 12.5 mm × 12.5 mm, the surface is placed in the middle, and it is composed of approximately 6 unit cells. Simulation parameters are $\Delta t = 63.4$ fs, $\Delta x = \Delta z = 53.75\ \mu$m ($\Lambda_x/40$, $\lambda_0/97$), the simulation runs over 750 ps, and the excitation is a Gaussian pulsed plane wave of amplitude 1 V/m and bandwidth of 15 GHz, centered at 57.5 GHz, and $N_{\text{FFT}} = 100$. Figure 4(a) shows the transmission and reflection magnitudes and phases between TD-only and TDSD cases. The importance of SD is clear when looking at the transmission depth profile shifting from 60GHz to 55 GHz. Moreover, Fig. 4(b) shows a good agreement between the analytical data from (6) and the Mixed GSTC-FDTD-TDSD proposed method. Insets show maximum absolute errors of 2.54 dB and 8.25° for magnitude and phase, respectively, closer to the edges of the characterization bandwidth.

The Huygens' metasurface data is presented in Tab. 4 and this time includes terms up to the sixth order in k_x along with constant susceptibility terms for both electric and magnetic, and is, therefore, a good candidate to test the capabilities of the proposed method. The dimensions of the simulation region are the same as that of the dipole structure, and the simulation parameters are $\Delta t = 39.15$ fs, $\Delta x = 52.5\ \mu$m ($\Lambda_x/40$, $\lambda_0/90$), $\Delta z = 26.25\ \mu$m ($\lambda_0/180$) and $N_{\text{FFT}} = 100$. The simulation runs over 2 ns, and the excitation is a Gaussian pulsed plane wave of amplitude 1 V/m and bandwidth of 5 GHz, centered at 63.5 GHz, therefore spanning over both electric and magnetic susceptibilities temporal resonances. Figure 5(a) presents the results for transmission and reflection coefficient across frequency and different angles of incidence for time dispersion only (top row, $k_x = 0$) and the case where both time and space dispersion are present. Again, these plots show the importance of including SD for cases of oblique incidence. Furthermore, Fig. 5(b) shows a good agreement between analytical results and the proposed Mixed GSTC-FDTD-TDSD method. Insets show maximum absolute errors

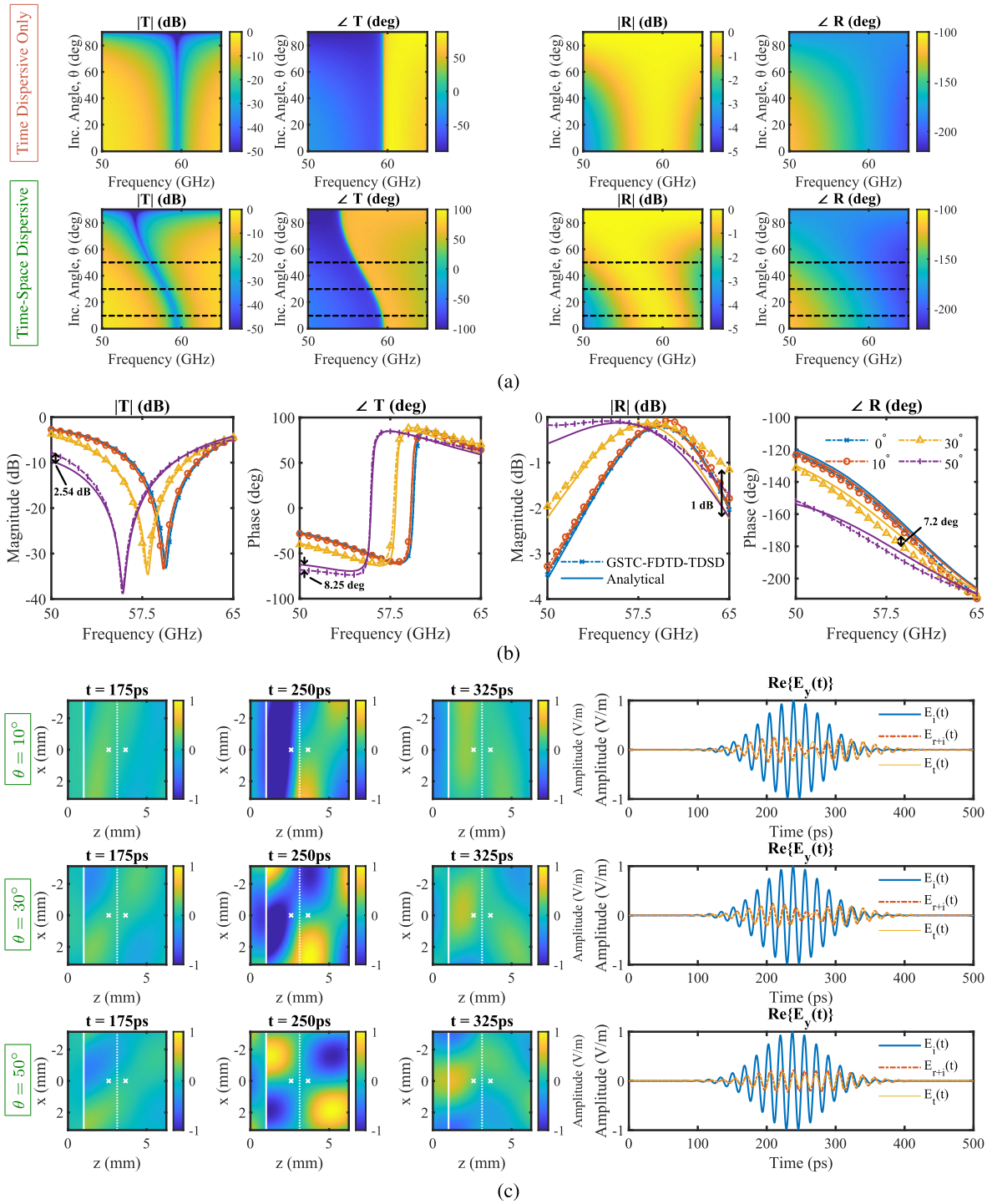

FIGURE 4. **(a) Analytical comparison of transmission and reflection magnitudes (dB) and phases (deg) for a uniform metasurface made of electric dipole cells with susceptibilities defined by the parameters in Tab 3 and a magnetic susceptibility modeled using a temporally-dispersive-only Drude model with $\omega_p = 4.9119 \times 10^9$ rad/s and $\gamma = 0.98 \times 10^9$ rad/s. The top panels show the analytical data for time dispersive susceptibilities ($\chi(\omega)$), and the bottom panels show data for a time and space dispersive scenario ($\chi(\omega, k_x)$). (b) Transmission and reflection where solid lines are analytical data obtained from (6), and marked dot-dashed lines are the results obtained from the Mixed GSTC-FDTD-TDSD algorithm. Line markers denote the angle of incidence. Arrow insets show the maximum absolute error. (c) The amplitude of the real part of the electric field over time. Image panels show field snapshots over the simulation region for three different angles of incidence and three different time instants. The insets show the source plane location (white solid line), the metasurface location (white dashed line), and the location of the reflection and transmission point monitors (white 'x' markers).**

of 4.93 dB and 20° for magnitude and phase, respectively, closer to the edges of the characterization bandwidth. Deviations start to occur as the angles approximate 50° where the propagation angle of the incidence field starts to be

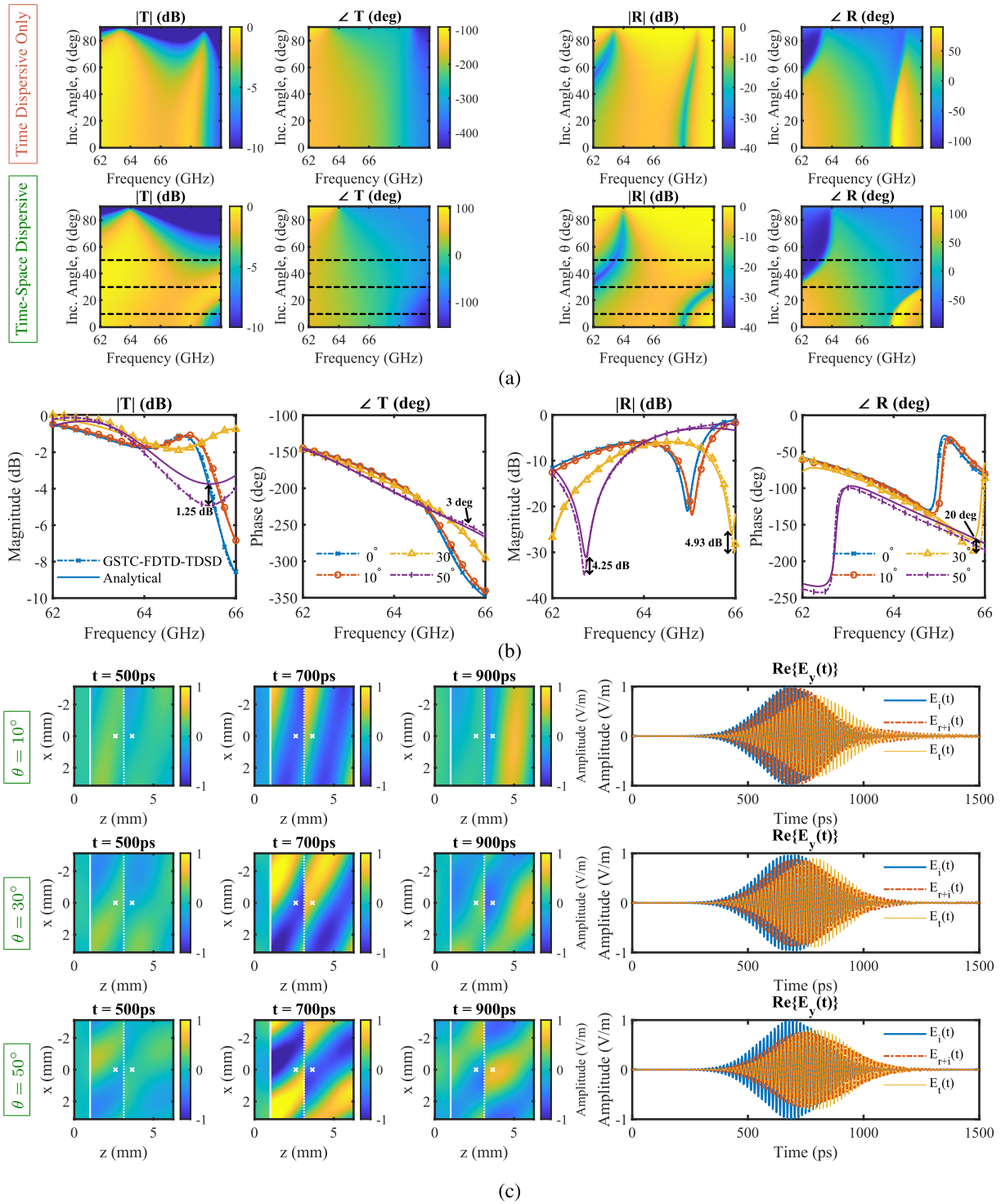

FIGURE 5. (a) Analytical comparison of transmission and reflection magnitudes (dB) and phases (deg) for a uniform metasurface composed of Huygens' all-dielectric cells with susceptibilities defined by the parameters in Tab 4. The top panels show the analytical data for time dispersive susceptibilities ($\chi(\omega)$), and the bottom panels show data for a time and space dispersive scenario ($\chi(\omega, k_x)$). (b) Transmission and reflection where solid lines are analytical data obtained from (6), and marked dot-dashed lines are the results obtained from the Mixed GSTC-FDTD-TDSD algorithm. Line markers denote the angle of incidence. Arrow insets show the maximum absolute error. (c) The amplitude of the real part of the electric field over time. Image panels show field snapshots over the simulation region for three different angles of incidence and three different time instants. The insets show the source plane location (white solid line), the metasurface location (white dashed line), and the location of the reflection and transmission point monitors (white 'x' markers).

disturbed by the constant phase shift of the center frequency imposed by the periodic boundary conditions.

The image panels in Figures 4(c) and 5(c) show the real part of E_y over the simulation region for three different

time instants and angles of incidence. The annotations show the locations of the source injection plane, the location of the metasurface, and the location of the point monitors for reflection and transmission fields that are depicted over time in the last plots to the right. Within the reflection region between the source and the metasurface, we can see a standing wave pattern caused by the interference of the source forward traveling wave, and the metasurface reflected backward traveling wave. Also, more pronounced in the transmission region, we see an intricate pattern that, due to the particular phase profile at different angles and frequencies, causes several plane waves to superimpose and not form the regular plane-wave profile that would be seen for a single plane wave excitation in a non-dispersive case.

The limitation in the angular resolution for the presented results is related to the type of soft source implemented in the algorithm and periodic boundary conditions (PBC). As the PBC contains a fixed transverse phase-shift determined by the center frequency ($k_x = k_0 \sin\theta$), the condition $k_0^2 = k_x^2 + k_z^2$ will force lower frequencies to propagate at a higher angle while higher frequencies will propagate at a lower angle [31]. For instance, Fig. 6 shows the error in the propagation angle for the incident signal in the wire dipole simulation, with up to $\pm 4°$ compared to the propagation of the center frequency at 57.5 GHz. Therefore justifying the angle limitations in the FDTD simulations presented in this work.

Overall, the analytical data presented in both metasurfaces take into account the propagation angle dictated by the PBC, but numerically, in the FDTD algorithm, those frequencies are injected at a specified angle and then converted to a different propagation direction as they propagate and reach the PBC edges. Therefore, deteriorating the solution at the edges of the bandwidth and at higher excitation angles where the results tend to be less accurate.

Possible solutions to this problem rely on using the Total-Field Scattered-Field source approach [22], [23], [32], [33], [34], or the split-field method, sometimes referred to as Broadband Fixed Angle Source Technique (BFAST) [35], [36]. The former relies on the study of finite metasurfaces within the total-field region and subsequent edge effects that might be related to the *effective* surface thickness within the FDTD framework. It does not solve the case of periodic boundary conditions but allows the excitation at grazing angles while the outer scattered region is surrounded by absorbing boundary conditions. The latter requires a different formulation of the regular Yee-cells, which would need to be extended to the GSTCs as well. Both are not part of the scope of this work and are left as future work.

A preliminary analysis of the code for the examples presented showed that the solution improves with a finer time and space step. Accurate results were obtained with time steps based on a Courant factor of 1/2, which is slightly lower than the stability condition of $\sqrt{2}$ reported in the literature for a standard 2D-FDTD solver [22], and space steps below

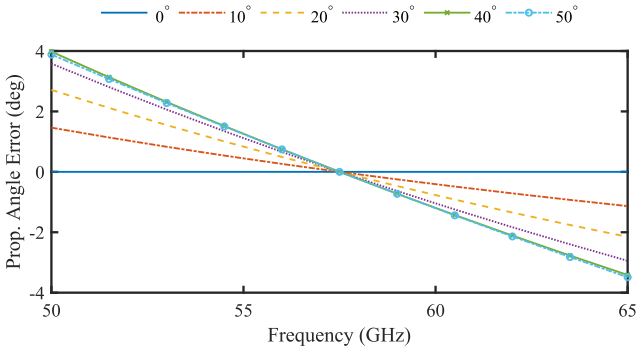

FIGURE 6. Propagation angle error compared to the propagation angle of the center frequency for the wire dipole surface. Different colors correspond to different plane wave incidence angles.

$\lambda_0/50$, which agrees with results reported in [12]. The value of N_{FFT} determines the accuracy of the solution in terms of angular resolution in the k_x domain. As stated before, due to the fixed phase shift of the PBCs, different frequencies will propagate at different angles, and this contributes to the spreading of the spectrum across discrete bins in the Fourier domain. Higher values of N_{FFT} will then improve the angular resolution, improving the evaluation of the interacting fields with the susceptibilities transfer functions.

Overall, this method is more memory efficient than the previous one, when the Lorentz coefficients order is greater than 2 ($n_d > 2$). In terms of CPU time, it is slower due to the extra FFT computations required at each time step. However, this performance can be boosted by solving multiple propagating wavenumbers in parallel, which is not possible in the case of the GSTC-FDTD-TDSD method where the coupled system of equations has to be solved all together. Section S3 of the Supplementary Material provides more details about the performance comparison.

VI. CONCLUSION

For the first time, a zero-thickness model of temporally and spatially dispersive metasurfaces was integrated into a finite-difference time-domain model. The proposed method extended the implicit Lorentzian model for a tight asymmetrical Yee cell in [12] to accommodate the spatial derivatives of the polarization terms and average fields on the surface via the *polynomial expansion* of the Lorentz parameters with respect to the transverse wavevector. The results were validated for oblique plane-wave incidence under a synthetic spatial dispersion response for both electric and magnetic tangential susceptibilities. Limitations in the extension of the method to higher-order expansion terms for the extended Lorentz model and poor conditioning of the characteristic matrix led to the development of a mixed finite-difference spatial-frequency-domain/time-domain method that solves the unknowns in the surface in the spatial frequency domain at every time step. This method was then validated by replicating the results for the spatiotemporal physical dispersive cells: the wire dipole and dielectric puck from [1].

This method contemplates constant polarization terms and is easily extendable to higher-order terms in the polynomial expansion of the Lorentz terms with respect to the transverse wavevector. Furthermore, the proposed method can be easily integrated into the standard FDTD solver since there is minimal disruption to the regular update equations for a Yee-cell-based solver.

An interesting path to follow in the future, and where the GSTC-FDTD framework becomes essential, is the analysis of spatiotemporal modulated surfaces similar to time modulated ones in [20], except that now the extended polynomial parameters of the Lorentz model can be functions of space for nonuniform surfaces, transverse wavevector for a spatial non-local response and also time due to the time modulation feature of the metasurface. This will, in practice, represent a linear time and space-variant (LTSV) system. In this matter, an FDTD framework will show even more importance when analyzing transient responses as the spatial dispersion of the surface changes over time.

Finally, the whole analysis performed in this work and its previous parts [2], [3], [37] can be applied to a general angular response in a 3D framework for finite-sized surfaces, both flat and conformal, where, assuming the propagation along z direction, the surface spatial dispersion would be characterized in terms of the transverse wave vector components k_x and k_y.

REFERENCES

[1] J. G. N. Rahmeier, T. J. Smy, J. Dugan, and S. Gupta, "Zero thickness surface susceptibilities and extended GSTCs—Part I: Spatially dispersive metasurfaces," *IEEE Trans. Antennas Propag.*, vol. 71, no. 7, pp. 5909–5919, Jul. 2023.

[2] T. J. Smy, J. G. N. Rahmeier, J. Dugan, and S. Gupta, "Spatially dispersive metasurfaces—Part II: IE-GSTC-SD field solver with extended GSTCs," *IEEE Trans. Antennas Propag.*, vol. 71, no. 7, pp. 5920–5934, Jul. 2023.

[3] J. Dugan, J. G. N. Rahmeier, T. J. Smy, and S. Gupta, "Spatially dispersive metasurfaces—Part III: Zero-thickness modeling of periodic and finite nonuniform surfaces," *IEEE Trans. Antennas Propag.*, vol. 71, no. 7, pp. 5935–5945, Jul. 2023.

[4] C. L. Holloway, E. F. Kuester, J. A. Gordon, J. O'Hara, J. Booth, and D. R. Smith, "An overview of the theory and applications of metasurfaces: The two-dimensional equivalents of metamaterials," *IEEE Antennas Propag. Mag.*, vol. 54, no. 2, pp. 10–35, Apr. 2012.

[5] H. Li, H. Zhang, and Y. Mu, "Spatial multiplexing complex amplitude holographic metasurface," in *Proc. Int. Conf. Microw. Millim. Wave Technol. (ICMMT)*, May 2021, pp. 1–3.

[6] T. J. Smy and S. Gupta, "Surface susceptibility synthesis of metasurface skins/holograms for electromagnetic camouflage/illusions," *IEEE Access*, vol. 8, pp. 226866–226886, 2020.

[7] S. Sakurai, J. G. N. Rahmeier, T. Tomura, J. Hirokawa, and S. Gupta, "Millimeter-wave Huygens' transmit arrays based on coupled metallic resonators," *IEEE Trans. Antennas Propag.*, vol. 69, no. 5, pp. 2686–2696, May 2021.

[8] K. Yee, "Numerical solution of initial boundary value problems involving Maxwell's equations in isotropic media," *IEEE Trans. Antennas Propag.*, vol. AP-14, no. 3, pp. 302–307, May 1966.

[9] N. Homsup, "A comparison between a spline-based method and a high-order FDTD scheme for the Maxwell equations," in *Proc. Int. Conf. Comput. Electromagn. Appl. (ICCEA)*, Nov. 1999, pp. 56–59.

[10] N. Homsup, "An adaptive higher-order FDTD scheme for electromagnetic problems," in *Proc. IEEE Southeast Conf. Preparing New Millennium*, Apr. 2000, pp. 177–181.

[11] A. K. Saxena and K. V. Srivastava, "Higher order LOD-FDTD methods and their numerical dispersion properties," *IEEE Trans. Antennas Propag.*, vol. 65, no. 3, pp. 1480–1485, Mar. 2017.

[12] T. J. Smy, S. A. Stewart, J. G. N. Rahmeier, and S. Gupta, "FDTD simulation of dispersive metasurfaces with Lorentzian surface susceptibilities," *IEEE Access*, vol. 8, pp. 83027–83040, 2020.

[13] X. Jia, X. Liu, F. Yang, M. Li, and S. Xu, "FDTD simulation of metasurfaces with generalized sheet transition conditions," in *Proc. Int. Appl. Comput. Electromagn. Soc. Symp. (ACES)*, Aug. 2017, pp. 1–2.

[14] X. Du, H. Yu, M. Li, and R. Chen, "Simulation of all-dielectric metasurfaces with finite thickness based on FDTD-GSTC," in *Proc. Int. Appl. Comput. Electromagn. Soc. Symp. (ACES)*, Jul. 2018, pp. 1–2.

[15] D. Mu, Y. Wang, and Q. Cao, "Analysis of metasurface to modulate EM waves based on the GSTC-FDTD method," in *Proc. Int. Appl. Comput. Electromagn. Soc. Symp. (ACES)*, Aug. 2019, pp. 1–2.

[16] D. Mu, Y. Wang, and Q. Cao, "Analysis of controllable metasurface using the GSTC-FDTD method," in *Proc. IEEE Int. Conf. Comput. Electromagn. (ICCEM)*, Mar. 2019, pp. 1–3.

[17] T. J. Smy and S. Gupta, "Finite-difference modeling of broadband Huygens' metasurfaces based on generalized sheet transition conditions," *IEEE Trans. Antennas Propag.*, vol. 65, no. 5, pp. 2566–2577, May 2017.

[18] K. Hosseini and Z. Atlasbaf, "PLRC-FDTD modeling of general GSTC-based dispersive bianisotropic metasurfaces," *IEEE Trans. Antennas Propag.*, vol. 66, no. 1, pp. 262–270, Jan. 2018.

[19] S. Jang, J. Cho, and K.-Y. Jung, "Efficient dispersive GSTC-FDTD algorithm using the Drude dispersion model," *IEEE Access*, vol. 10, pp. 59486–59494, 2022.

[20] V. Tiukuvaara, T. J. Smy, and S. Gupta, "Floquet analysis of space–time modulated metasurfaces with Lorentz dispersion," *IEEE Trans. Antennas Propag.*, vol. 69, no. 11, pp. 7667–7678, Nov. 2021.

[21] X. Jia, X. Wang, and Y. Vahabzadeh, "Fast computation of resonant metasurfaces in FDTD scheme using dispersive surface susceptibility model," *IEEE Trans. Antennas Propag.*, vol. 71, no. 1, pp. 713–722, Jan. 2023.

[22] A. Taflove and S. C. Hagness, *Computational Electrodynamics: The Finite-difference Time-Domain Method*, 3rd ed. Norwood, MA, USA: Artech House, 2005.

[23] A. Z. Elsherbeni and V. Demir, *The Finite-Difference Time-Domain Method: Electromagnetics With MATLAB® Simulations*, 2nd ed. London, U.K.: IET, 2015.

[24] M. M. Idemen, *Discontinuities in the Electromagnetic Field*. Hoboken, NJ, USA: Wiley, 2011.

[25] K. Achouri, M. A. Salem, and C. Caloz, "General metasurface synthesis based on susceptibility tensors," *IEEE Trans. Antennas Propag.*, vol. 63, no. 7, pp. 2977–2991, Jul. 2015.

[26] M. K. Emara, T. Tomura, J. Hirokawa, and S. Gupta, "All-dielectric Fabry–Pérot-based compound Huygens' structure for millimeter-wave beamforming," *IEEE Trans. Antennas Propag.*, vol. 69, no. 1, pp. 273–285, Jan. 2021.

[27] M. K. Emara, T. Tomura, J. Hirokawa, and S. Gupta, "Fabry–Pérot-based compound all-dielectric Huygens' structure for circularly polarized millimeter-wave beamforming," *IEEE Antennas Wireless Propag. Lett.*, vol. 19, pp. 1784–1788, 2020.

[28] Mathworks. (2023). *Condition Number for Inversion*. [Online]. Available: https://www.mathworks.com/help/MATLAB/ref/cond.html

[29] I. S. Duff and J. Koster, "On algorithms for permuting large entries to the diagonal of a sparse matrix," *SIAM J. Matrix Anal. Appl.*, vol. 22, no. 4, pp. 973–996, Jan. 2001, doi: 10.1137/s0895479899358443.

[30] Mathworks. (2023). *Matrix Scaling for Improved Conditioning*. [Online]. Available: https://www.mathworks.com/help/MATLAB/ref/equilibrate.html

[31] Ansys Lumerical FDTD. (2023). *Understanding Injection Angles in Broadband Simulations*. [Online]. Available: https://optics.ansys.com/hc/en-us/articles/360034382894-Understanding-injection-angles-in-broadband-simulations

[32] J. B. Schneider and K. Abdijalilov, "Analytic field propagation TFSF boundary for FDTD problems involving planar interfaces: PECs, TE, and TM," *IEEE Trans. Antennas Propag.*, vol. 54, no. 9, pp. 2531–2542, Sep. 2006.

[33] K. Abdijalilov and J. B. Schneider, "Analytic field propagation TFSF boundary for FDTD problems involving planar interfaces: Lossy material and evanescent fields," *IEEE Antennas Wireless Propag. Lett.*, vol. 5, pp. 454–458, 2006.

[34] T. Tan, A. Taflove, and V. Backman, "A proposed perfectly matched stratified medium FDTD TFSF sourced by inhomogeneous plane waves," in *Proc. Int. Conf. Electromagn. Adv. Appl.*, Sep. 2011, pp. 921–924.
[35] B. Liang, M. Bai, H. Ma, N. Ou, and J. Miao, "Wideband analysis of periodic structures at oblique incidence by material independent FDTD algorithm," *IEEE Trans. Antennas Propag.*, vol. 62, no. 1, pp. 354–360, Jan. 2014.
[36] Ansys Lumerical FDTD. (2023). *Broadband Fixed Angle Source Technique (BFAST)*. [Online]. Available: https://optics.ansys.com/hc/en-us/articles/360034902273-Broadband-Fixed-Angle-Source-Technique-BFAST-
[37] J. Dugan, J. G. N. Rahmeier, Tom. J. Smy, and S. Gupta, "Non-uniform spatially dispersive metasurfaces as locally linear space invariant (LSI) systems," in *Proc. 17th Eur. Conf. Antennas Propag. (EuCAP)*, Mar. 2023, pp. 1–5.

JOÃO GUILHERME NIZER RAHMEIER (Member, IEEE) received the Bachelor of Science degree in electrical and electronics engineering from Universidade Federal do Pampa, Rio Grande do Sul, Brazil, in 2016, the Master of Science degree in microelectronics and microsystems from Universidade Federal de Minas Gerais, Minas Gerais, Brazil, in 2018, and the Ph.D. degree in electrical and computer engineering from Carleton University, Canada, in 2023. He is currently working on metasurfaces and computational electromagnetism with Carleton University. He is also a Research Scientist with Optiwave Systems Inc., Ottawa, ON, Canada, for the development of state-of-the-art computational electromagnetic simulation tools. He started his academic journey with Universidade Federal do Pampa. He was a Research Scholar for four years. As a master's student, he obtained an Honorable Mention in the Best Student Paper Competition Award of the 32nd Symposium on Circuits and Systems Design. He received the 2022 IEEE Antennas and Propagation Society Fellowship Award and the Best Student Paper Award at the 2023 European Conference on Antennas and Propagation. In addition to his academic and professional pursuits, he is an Active Volunteer as the Social Media Director (2019–2021) and the Vice-Chair (2022–2024) with the IEEE Young Professionals Ottawa, helping organize events and workshops in different subjects related to engineering and soft and hard skills.

JORDAN DUGAN received the B.S. and M.S. degrees in electrical engineering from Carleton University, in 2020, and 2022, respectively, where he is currently pursuing the Ph.D. degree with the Department of Electronics. His M.S. thesis on metasurfaces won the graduate award for top M.S. thesis in the school. He is also a Research Assistant with the Department of Electronics, Carleton University. His research interests include metasurfaces, electromagnetics, and computational physics.

TOM J. SMY received the B.Sc. and Ph.D. degrees in electrical engineering from the University of Alberta, Edmonton, AB, Canada, in 1986 and 1990, respectively. He is currently a Professor with the Department of Electronics, Carleton University, Ottawa, ON, Canada. He has authored or coauthored more than 100 journal articles. He has coauthored the OptiSpice, Atar, SIMBAD, and 3-D-Films simulators. His current research interests include the optical, thermal, and multiphysics simulation of electronic devices/packages and modules, the study and simulation of thin-film growth and microstructures, and the fundamental electromagnetic simulation of metasurfaces.

SHULABH GUPTA (Senior Member, IEEE) was born in Etah, India, in 1982. He received the B.Tech. degree in electronic engineering from the Indian School of Mines (IIT) at Dhanbad, Dhanbad, India, in 2004, the M.S. degree in telecommunications from Institut National de la Recherche Scientique, Énergie Matériaux Télécommunications Research Center, Université du Québec, Montreal, QC, Canada, in 2006, and the Ph.D. degree in electrical engineering from École Polytechnique of Montreal, Montreal, in 2012. From 2009 to 2010, he was a Visiting Research Fellow with the Tokyo Institute of Technology, Tokyo, Japan, and followed by a Postdoctoral Fellow with the University of Colorado at Boulder, Boulder, CO, USA, in 2012. He was also a Postdoctoral Fellow with The University of Hong Kong, Hong Kong, from 2012 to 2014, and École Polytechnique of Montreal, from 2014 to 2016. He is currently an Associate Professor with the Department of Electronics, Carleton University, Ottawa, ON, Canada. He is also a Licensed Professional Engineer of Ontario. He was a recipient of the Young Scientist Award of the International Symposium on Electromagnetic Theory Ottawa, in 2007, the International Union of Radio Science-General Assembly, Chicago, in 2008, and ISAP Jeju, in 2011. His thesis received the Best Doctoral Dissertation Award from École Polytechnique of Montreal, in 2012, the Prix d'excellence de l'Association des Doyens des Études Supérieures au Québec Edition, QC, Canada, in 2013, and the Academic Gold Medal of the Governor General of Canada.